HHS Public Access

Author manuscript

Neuron. Author manuscript; available in PMC 2018 July 19.

Published in final edited form as:

Neuron. 2017 July 19; 95(2): 281–296.e6. doi:10.1016/j.neuron.2017.06.026.

Loss of TMEM106B Ameliorates Lysosomal and Frontotemporal Dementia-Related Phenotypes in Progranulin-Deficient Mice

Zoe A. Klein[1,4], **Hideyuki Takahashi**[1,4], **Mengxiao Ma**[1], **Massimiliano Stagi**[1], **Melissa Zhou**[1], **TuKiet T. Lam**[2,3], and **Stephen M. Strittmatter**[1,*]

[1]Program in Cellular Neuroscience, Neurodegeneration & Repair, Departments of Neurology and of Neuroscience, Yale University School of Medicine, New Haven, CT

[2]Department of Molecular Biophysics and Biochemistry, Yale University, New Haven, CT

[3]MS & Proteomics Resource, WM Keck Biotechnology Resource Laboratory, New Haven, CT

SUMMARY

Progranulin (*GRN*) and *TMEM106B* are associated with several common neurodegenerative disorders including frontotemporal lobar degeneration (FTLD). A *TMEM106B* variant modifies *GRN*-associated FTLD risk. However, their functional relationship *in vivo* and the mechanisms underlying the risk modification remain unclear. Here, using transcriptomic and proteomic analyses with *Grn*−/− and *Tmem106b*−/− mice, we show that while multiple lysosomal enzymes are increased in *Grn*−/− brain at both transcriptional and protein levels, TMEM106B deficiency causes reduction in several lysosomal enzymes. Remarkably, *Tmem106b* deletion from *Grn*−/− mice normalizes lysosomal protein levels and rescues FTLD-related behavioral abnormalities and retinal degeneration, without improving lipofuscin, C1q or microglial accumulation. Mechanistically, TMEM106B binds vacuolar-ATPase accessory protein 1 (AP1). TMEM106B deficiency reduces vacuolar-ATPase AP1 and V0 subunits, impairing lysosomal acidification and normalizing lysosomal protein levels in *Grn*−/− neurons. Thus, *Grn* and *Tmem106b* genes have opposite effects on lysosomal enzyme levels, and their interaction determines the extent of neurodegeneration.

eTOC

Klein et al. study the role of frontotemporal dementia associated proteins in mouse models. Loss of Progranulin increases lysosomal enzymes, while TMEM106B loss lowers lysosomal pH and reduces levels. The double mutant rescues neurodegeneration observed with single Progranulin gene loss.

*Correspondence and lead contact: Stephen.Strittmatter@yale.edu.

[4]These authors contributed equally.

AUTHOR CONTRIBUTIONS

Z.A.K., H.T., and S.M.S. designed most experiments. Z.A.K. and H.T. collected most of the data, with assistance from M.Z. The TMEM106B null line was established by M.M. and M.S., while T.T.L. conducted mass spectrometric analysis. H.T., Z.A.K., and S.M.S. analyzed results and wrote the manuscript.

INTRODUCTION

Progranulin (PGRN) is a widely expressed secreted glycoprotein that plays a role in development, wound repair, and tumorigenesis. In the central nervous system, PGRN is expressed by neurons and microglia. Haploinsufficiency due to heterozygous loss-of-function mutations in the PGRN gene (*GRN*) is a frequent cause of familial frontotemporal lobar degeneration (FTLD)-TDP, the common FTLD subtype characterized by neuronal inclusions of TAR DNA-binding protein 43 (TDP-43) (Cenik et al., 2012; De Muynck and Van Damme, 2011; Petkau and Leavitt, 2014). Rare homozygous *GRN* mutations cause neuronal ceroid lipofuscinosis (NCL) (Smith et al., 2012). Several previous genetic studies have also suggested PGRN as a risk factor for Alzheimer's disease (AD), hippocampal sclerosis, and Gaucher disease (Dickson et al., 2010; Jian et al., 2016b; Jing et al., 2016).

TMEM106B was initially described as a risk modifier of FTLD-TDP by a genome-wide association study (GWAS) (Nicholson and Rademakers, 2016). FTLD-TDP risk association is increased in *GRN* mutation carriers where single-nucleotide polymorphisms (SNPs) in *TMEM106B* reduce disease penetrance (Finch et al., 2011; Van Deerlin et al., 2010). The *TMEM106B* risk allele is reportedly associated with lower PGRN levels (Cruchaga et al., 2011; Finch et al., 2011). Subsequently, *TMEM106B* has been found to be a protective genetic modifier against C9ORF72 expansion-causing FTLD (Gallagher et al., 2014; van Blitterswijk et al., 2014). *TMEM106B* SNPs may also modify the pathological presentation of AD (Rutherford et al., 2012). Several genetic studies have also reported a significant underrepresentation of the *TMEM106B* protective allele in hippocampal sclerosis patients (Murray et al., 2014; Nelson et al., 2015).

Despite an overlapping role of *GRN* and *TMEM106B* in neurodegenerative disorders, their functional relationship in the brain as well as the disease processes remains unknown. PGRN is thought to have neurotrophic and anti-inflammatory effects in the brain. However, recent studies also link PGRN to lysosomal biology. NCL and Gaucher diseases, in which PGRN is implicated, are lysosomal storage disorders. PGRN binds several lysosomal proteins such as sortilin, prosaposin, and β-glucocerebrosidase (Hu et al., 2010; Jian et al., 2016a; Zhou et al., 2015). Lysosomal proteins, which accumulate in NCL, have also been found to accumulate in FTLD-TDP patients with *GRN* mutations (Gotzl et al., 2014). TMEM106B is a transmembrane protein that localizes to the endo-lysosomal membrane (Brady et al., 2013; Chen-Plotkin et al., 2012; Lang et al., 2012). TMEM106B controls the size, number, motility, and trafficking of lysosomes in both neuronal and non-neuronal cells (Brady et al., 2013; Chen-Plotkin et al., 2012; Schwenk et al., 2014; Stagi et al., 2014). These studies suggest that PGRN and TMEM106B play a critical role in lysosomal biology. To date, TMEM106 loss-of-function has been investigated *in vitro*, and it remains unclear which brain phenotypes require TMEM106B *in vivo*. In addition, the interplay between PGRN and TMEM106B in the lysosome is yet to be determined.

To investigate effects of TMEM106B loss-of-function on brain function *in vivo* and its relationship to PGRN, we create TMEM106B-deficient (*Tmem106b*−/−) mice and perform transcriptomic and proteomic analyses using 2-month-old *Grn*−/− and *Tmem106b*−/− mice.

While lysosomal dysregulation is the most prominent early change found in *Grn*−/− brain at both transcriptional and protein levels, *Tmem106b*−/− brain shows opposite changes in several lysosomal enzymes at the protein level. Given the opposite protein changes in null mice and the genetic interaction in FTLD-TDP, we crossed these mouse strains. Remarkably, TMEM106B deficiency not only normalizes the lysosomal protein dysregulation but also rescues FTLD-related behavioral deficits and retinal degeneration in *Grn*−/− mice. We show that TMEM106B interacts with V-ATPase and its deficiency causes downregulation of V-ATPase V0 domain, impairment in lysosomal acidification, and thereby normalizes lysosomal enzyme activity in *Grn*−/− neurons. These results provide novel insights into TMEM106B biology in the brain, the functional connection between *Grn* and *Tmem106b*, and neurodegenerative disorders related to these proteins including FTLD-TDP.

RESULTS

Transcriptomic and proteomic analyses reveal global lysosome dysfunction in *Grn*−/− brain

Grn−/− mice recapitulate several features of PGRN-deficient FTLD as well as NCL, including accumulation of lipofuscin, microgliosis, and retinal degeneration while *Grn*+/− mice do not (Ahmed et al., 2010; Filiano et al., 2013; Hafler et al., 2014; Petkau et al., 2012; Yin et al., 2010a; Yin et al., 2010b). Therefore, the PGRN null mice have been used as the best available experimental mouse model for these disorders.

In order to examine early global alterations occurring in 2-month-old *Grn*−/− brain at both transcriptional and protein levels, we performed genome-wide RNA sequencing (RNASeq) and a Label-Free Quantitation Liquid Chromatography Mass Spectrometry (LFQ-LCMS). The proteomic technique calculated levels based on the normalization to the total protein abundance in each sample with a False Discovery Rate of < 1% (Figure 1A). The RNASeq and LFQ-LCMS analyses identified 958 genes and 256 proteins differentially expressed (DE), respectively, between WT versus *Grn*−/− brains. We then performed gene ontology (GO) analysis of the DE species in both analyses using KEGG pathways. Interestingly, in the both cases, the GO analysis identified lysosome as the most significantly enriched term after Bonferroni correction with 14 and 8 genes identified as part of the pathway in RNASeq and LFQ-LCMS, respectively (Figure 1B). We therefore compared all DE genes identified by RNASeq and LFQ-LCMS with 364 mouse lysosomal genes on The Mouse Lysosomal Gene Database (http://lysosome.unipg.it/mouse.php), and identified 29 and 19 DE lysosomal genes in RNASeq and LFQ-LCMS, respectively. Notably, most lysosomal genes identified are upregulated in both analyses (24 out of 29 in RNASeq and 17 out of 19 in LFQ-LCMS) (Figure 1C). The DE lysosomal genes include Cathepsins (Cat) CatD, CatS, CatB, CatC, and CatZ and lysosomal-associated membrane protein 1 (LAMP1) and LAMP2 and β subunit of hexosaminidase (Hex) in protein names in RNASeq (Figure 1D and Table S1). In addition to CatB and CatL, tripeptidyl-peptidase 1 (TPP1) and dipeptidyl-peptidase 2 (DPPII) were also in the DE lysosomal genes in LFQ-LCMS analysis (Figure 1E and Table S2). These transcriptomic and proteomic analyses clearly suggest lysosomal dysregulation as one of the earliest global changes occurring in *Grn*−/− brain at both transcriptional and protein levels.

As PGRN is thought to be involved in microglial neuroinflammation, we also analyzed typical microglial pro- and anti-inflammatory genes including IL1β, iNOS, and TGFβ as well as common microglial markers such as Iba1 and CD11b using our RNASeq dataset. Interestingly, none of these genes and markers is significantly changed or detected in our RNASeq analysis (Table S3). Recent transcriptome analysis of *Grn−/−* mice has shown that the complement pathway is upregulated (Lui et al., 2016). Our KEGG analysis also identified the complement pathway as it relates to *S. Aureus* infection (Figure 1B). In addition, using the STRING protein-protein interaction network analysis (von Mering et al., 2003) of our RNASeq dataset, we found transcriptional upregulation of several complement proteins including C1q as a part of microglial TYROBP network genes (TNG) caused by PGRN deficiency (Figure S1) (Takahashi et al., 2017). Together, these results suggest that PGRN deficiency has no effects on typical microglial pro- and anti-inflammatory genes but does induce transcriptional upregulation of microglial TNG including C1q beginning at 2 months of age.

PGRN deficiency causes early and sustained lysosomal enzyme dysregulation

To validate the findings of the RNASeq and LFQ-LCMS analyses, we first performed immunoblot analysis using 2-month-old WT and *Grn−/−* brain lysates. Immunoblots for DPPII, CatB, CatL, and LAMP1 show a significant increase in these lysosomal enzymes in *Grn−/−* brain (Figure 2A and 2B). We next examined the magnitude of lysosomal enzyme changes over the course of the animal's lifetime. For immunohistochemistry, we quenched autofluorescent signal by copper sulfate treatment prior to imaging (Schnell et al., 1999). Immunostaining for DPPII shows a significant increase in the immunoreactive area in both thalamus and cortex of *Grn*−/− mice, largely driven by increase in number of DPPII-positive puncta (Figure 2C–F). Double immunofluorescence with anti-NeuN antibody shows predominant neuronal accumulation of DPPII (Figure 2D). In addition, the magnitude of increase in DPPII-positive area does not change from 2 months of age to 12 months of age in the cortex but increases slightly by 12 months of age in the thalamus (Figure 2E and 2F). We also measured lysosomal enzyme activities using WT and *Grn*−/− brain lysates. Consistent with the biochemical and immunohistological analyses, CatB, DPPII, and Hex A/B/S enzyme activities in *Grn*−/− brain lysate are also increased after 2 months of age and the increased activities are sustained through 13 months of age, suggesting that the increased lysosomal enzymes in *Grn*−/− brain are properly folded and functional (Figure 2G–I). Furthermore, these lysosomal enzyme changes are not found in P15 *Grn*−/− brain, excluding the possibility of a developmental defect for these pathways in *Grn*−/− mice (Figure 2E–I).

To evaluate lysosomal enzyme function, we measured total protein degradation in *Grn*−/− primary cultured cortical neurons using a [^{3}H] leucine pulse-chase method (Kaushik and Cuervo, 2009). PGRN deficiency significantly increases lysosomal proteolysis in primary cultured cortical neurons (Figure 2J). Finally, we assessed lipofuscin deposition, an indicator of lysosomal dysregulation, and found that it accumulates at 2 months of age in *Grn−/−* mice in both the cortex and thalamus, with the most robust changes occurring in the thalamus (Figure 2K and 2L, Figure S2). Thus, altered lysosomal enzyme amount and activity start in early adulthood and do not change appreciably as other abnormalities, such as microgliosis,

develop at later ages (Ahmed et al., 2010; Filiano et al., 2013; Petkau et al., 2012; Yin et al., 2010a; Yin et al., 2010b).

TMEM106B and PGRN bidirectionally control lysosomal biology *in vivo*

Although TMEM106B has also been reported to localize at the lysosome and function as a regulator of lysosomal size, stability, and motility *in vitro* (Brady et al., 2013; Chen-Plotkin et al., 2012; Stagi et al., 2014), its *in vivo* role in the brain and its relationship to PGRN remain unclear. To address these questions, we generated *Tmem106b*−/− mice (Figure S3A). Quantitative real-time PCR using a probe directed against exons 3 and 4 confirms the absence of mature *Tmem106b* transcript in the mice (Figure S3B and S3C). *Tmem106b*+/− mice show a comparable level of TMEM106B mRNA, suggesting the presence of compensatory mechanisms of TMEM106B upregulation upon deletion of one *Tmem106b* allele (Figure S3C). Immunoblot of detergent-soluble fractions from WT and *Tmem106b*−/− brains shows depletion of the 70 kDa immunoreactive band specifically in *Tmem106b*−/− brain (Figure S3D). Consistent with a previous study (Chen-Plotkin et al., 2012), the immunoreactive bands are lost after heat treatment (Figure S3E). *Tmem106b*−/− mice are born in expected Mendelian ratio and appear phenotypically normal.

To characterize the *Tmem106b*−/− brain at the transcriptional and protein levels, we performed RNASeq and LFQ-LCMS analyses of 2-month-old *Tmem106b*−/− brain (Figure 3A). Surprisingly, RNASeq analysis shows minimal changes (54 DE genes between WT versus *Tmem106b*−/−) and the only differentially expressed lysosomal gene amongst 364 mouse lysosomal genes was TMEM106B itself (Figure 3B and Table S4). Thus, TMEM106B deficiency does not transcriptionally regulate the lysosome at 2 months of age. We also observed no significant transcriptional changes in microglial pro- and anti-inflammatory genes or the TNG (Table S5). However, LFQ-LCMS protein analysis revealed that multiple lysosomal enzymes, which we previously found to be upregulated in *Grn*−/− brain (Figure 1), are downregulated in *Tmem106b*−/− brain. Among the proteins that changed in the opposite direction are the proteases CatB, CatL, and DPPII (Figure 3C and 3D), suggesting that *TMEM106B* and *GRN* exert bidirectional control over several lysosomal proteins *in vivo*.

Loss of TMEM106B rescues dysregulation of several lysosomal enzymes in *Grn*−/− mice

Given the opposing lysosomal protein phenotypes in the two null mouse lines and the human genetic interaction (Finch et al., 2011; Van Deerlin et al., 2010), we sought to test whether TMEM106B deficiency modulates lysosome enzyme dysregulation in *Grn*−/− mice. Consistent with LFQ-LCMS, immunoblot of 5-month-old mice confirms a significant decrease in DPPII and CatB levels in *Tmem106b*−/− brain, while *Grn*−/− samples show a significant increase in these proteins levels. Strikingly, the double knockout *Grn*−/− *Tmem106b*−/− brain has normalized DPPII and CatB levels equal to WT levels. While LAMP1 is not significantly different in *Grn*−/− mice at this age, *Tmem106b*−/− samples have decreased LAMP1 levels and in the *Grn*−/− *Tmem106b*−/− brain, LAMP1 levels are normalized, indicating that TMEM106B and PGRN interact to control LAMP1 (Figure 4A and 4B). At the immunohistological level, staining for DPPII in 5-month-old *Grn*−/− *Tmem106b*−/− brain reveals that the increase in DPPII-positive area and puncta in thalamus

and cortex of *Grn*−/− mice is fully normalized by loss of TMEM106B (Figure 4C–E). We also examined whether loss of TMEM106B affects increased lysosomal enzymatic activities caused by PGRN deficiency. Interestingly, while increased CatB and DPPII enzyme activities in 7-month-old *Grn*−/− brain lysate are normalized by TMEM106B deficiency, no significant changes are observed for Hex A/B/S activity (Figure 4F–H), suggesting that TMEM106B deficiency rescues most but not all lysosomal enzyme activities. The DPPII and TPP1 activities measured in primary neuronal cultures also show a significant decrease in their activity in *Tmem106b*−/− and/or *Grn*−/− *Tmem106b*−/− compared to *Grn*−/− (Figure 4I and 4J). At the functional level, a pulse-chase experiment shows that lysosomal proteolysis of *Grn*−/− *Tmem106b*−/− primary cultured cortical neurons is comparable to that of WT neurons (Figure 4K). Together, these observations demonstrate that loss of TMEM106B normalizes the prominent *Grn* null phenotype of elevated lysosomal enzyme and proteolysis.

TMEM106B deficiency causes impairment in lysosomal acidification

We next sought to understand the mechanism by which TMEM106B deficiency normalizes the lysosomal enzyme dysregulation. As TMEM106B deficiency has no significant effect on transcriptional levels (Figure 3B), the normalization we observe in double deletion *Grn*−/− *Tmem106b*−/− mice must occur at the protein level. Confirming the RNAseq results, quantitative real-time PCR analyses show that loss of TMEM106B has no significant effect on transcriptional upregulation of several lysosomal genes in *Grn*−/− mice even at 7 months of age (Figure S4A). We thus analyzed the intersection of DE proteins in *Tmem106b*−/− mice identified by LFQ-LCMS analysis with 364 mouse lysosomal genes. We observed that vacuolar-ATPase (V-ATPase) V0 domain subunits V0a1, V0c, and V0d1 and accessary protein 1 (AP1) are significantly downregulated in *Tmem106b*−/− mice (Figure 5A–C). These V0 subunits are not significantly altered in *Grn*−/− brain in either the RNASeq or the LFQ-LCMS datasets (Figure 5C and Figure S5A). The LFQ-LCMS dataset also shows no significant increase in V-ATPase V1 subunits in *Grn*−/− brain (Figure S5B). These results demonstrate that PGRN deficiency has no effect on V-ATPase levels and changes in V-ATPase V0 domain subunits are caused selectively by TMEM106B loss.

As V-ATPase is responsible for lysosomal acidification (Colacurcio and Nixon, 2016; Cotter et al., 2015; Forgac, 2007; Mindell, 2012; Toei et al., 2010), we examined whether TMEM106B deficiency affects lysosomal acidification in primary cultured cortical neurons by using the pH-sensitive dye LysoTracker Red DND-99 (Busch et al., 2016; Chen-Plotkin et al., 2012) (Figure S6A). *Tmem106b*−/− neurons survive in culture and develop normal morphology as detected by MAP2 staining (Figure 5E and 5I). However, TMEM106B deficiency significantly reduces LysoTracker-positive lysosomal area despite a comparable cell density between WT and *Tmem106b*−/− neurons (Figure 5D, 5F, 5I, Figure S6B and S6C). Not only is acidified lysosomal area decreased, but the fluorescent intensity detected within this area by LysoTracker is also decreased significantly by loss of TMEM106B (Figure 5G, Figure S6B and S6C). There is a 15–20% decrease in integrated intensity of lysoTracker signal in neurons lacking TMEM106B (Fig. 5H and Fig. S6B and S6C). Thus, TMEM106B deficiency impairs lysosomal acidification.

These results led us to hypothesize that downregulation of V-ATPase V0 domain and impairment in lysosomal acidification by TMEM106B deficiency destabilizes several lysosomal enzymes and normalizes protein levels in *Grn*−/− mice. To test whether impaired acidification is sufficient, we examined the effects of Bafilomycin A1 (BafA1), a V-ATPase inhibitor (Yoshimori et al., 1991; Zhang et al., 1994), on DPPII and TPP1 enzyme activities and lysosomal proteolysis in *Grn*−/− primary cultured cortical neurons. Treatment with BafA1 for 2 days significantly decreases DPPII and TPP1 enzyme activity and lysosomal proteolysis in *Grn*−/− neurons (Figure S7A–C). These results suggest that impairment in lysosomal acidification can decrease lysosomal enzyme activity and proteolysis in the *Grn*−/− background, supporting the hypothesis for TMEM106B action in double knockout brain via V-ATPase regulation.

TMEM106B interacts with V-ATPase AP1

Given that TMEM106B deficiency causes downregulation of V-ATPase V0 domain subunits and AP1 as well as an impairment in lysosomal acidification, we examined whether TMEM106B physically interacts with V-ATPase to stabilize the protein. We first performed co-immunoprecipitation (co-IP) assay using HEK293T cells expressing TMEM106B-GFP and myc-DDK-tagged V-ATPase V0 domain and AP1 subunits. Interestingly, myc-DDK-tagged V-ATPase AP1 is strongly co-immunoprecipitated with TMEM106B-GFP while myc-DDK-tagged V-ATPase V0 domain subunits V0c and V0d1 are only weakly co-immunoprecipitated with TMEM106B-GFP (Figure 6A and 6B), suggesting that TMEM106B binds V-ATPase via AP1. We were unsuccessful in overexpressing V-ATPase V0a1 (data not shown). As a lysosomal protein control, myc-DDK-tagged CatB is not co-immunoprecipitated with TMEM106B-GFP (Figure 6A and 6B). Endogenous V-ATPase AP1 in HEK293T cells is also co-immunoprecipitated with TMEM106B-mCherry (Figure 6C and 6D). Mapping experiments using GFP-tagged TMEM106B lacking either the N-terminal or C-terminal region (ΔN or ΔC) show a significant decrease (> 50%) in co-IP of myc-DDK-tagged V-ATPase AP1 with ΔC TMEM106B-GFP while the N-terminal deletion has no significant effects on their interaction (Figure 6E–G). These results suggest that lumenal segment of TMEM106B contributes substantially to TMEM106B interaction to V-ATPase AP1. Incomplete loss of co-IP of V-ATPase AP1 by the C-terminal deletion however also suggests that the transmembrane domain participates in the protein association as well. Thus, physical interaction of TMEM106B and V-ATPase AP1 provides a mechanism for regulation of lysosomal acidification by loss of TMEM106B.

Loss of TMEM106B does not rescue the lipofuscin, CD68-positive microglia, and complement C1q phenotypes in *Grn*−/− brain

Because TMEM106B deficiency rescues certain aspects of lysosomal enzyme dysregulation in *Grn*−/− mice, we sought to clarify whether TMEM106B deficiency would prevent accumulation of lipofuscin in 5-month-old *Grn*−/− mice. *Tmem106b*−/− mice do not show any change in deposition of lipofuscin compared to WT mice. Furthermore, TMEM106B deficiency has no significant effect on accumulation of lipofuscin in *Grn*−/− mice (Figure 7A and 7D).

As previous studies have shown an increase in microglial TNG including CD68 and complement C1q in *Grn*−/− mice (Figure S1) (Lui et al., 2016; Takahashi et al., 2017), we also examined whether *Tmem106b* deletion affects accumulation of CD68-positive microglia and C1q deposition in *Grn*−/− mice. Quantitative real-time PCR analyses show that loss of TMEM106B does not prevent transcriptional upregulation of C1qA and C1qB in 7-month-old *Grn*−/− mice (Figure S4B). CD68 and C1q immunostaining show that TMEM106B deficiency does not revert the increase in either CD68-immunoreactive area (Figure 7B and 7E) or C1q immunoreactivity (Figure 7C and 7F) in the cortex of *Grn*−/− mice at 5 months of age. Thus, TMEM106B removal selectively corrects only certain phenotypes in *Grn*−/− mice.

TMEM106B deficiency rescues behavioral phenotypes in *Grn*−/− mice

Given the divergent ability of TMEM106B deficiency to rescue lysosomal protein levels but not lipofuscinosis, microglial or complement phenotypes, we sought to determine the consequences for brain function and degeneration. At 4 months of age, *Grn*−/− mice showed a statistically significant increase in locomotor activity in the open field behavior test as compared to WT mice. In contrast, *Tmem106b*−/− mice did not show any significant change in locomotor activity compared to WT. Interestingly, *Grn*−/− *Tmem106b*−/− mice exhibit a rescue of hyperactivity, demonstrating that *Grn* and *Tmem106b* interact to control behavior (Figure 8A).

FTLD patients have been reported to show an increased level of disinhibition (de Vugt et al., 2006). We therefore also examined behavior of 4-month-old *Grn*−/− mice in the context of the elevated plus maze. Mice generally prefer the enclosed arms of the maze and spend less time in the open arms. Mice that show disinhibition spend more time in the open arms of the maze. *Grn*−/− mice enter the open arms of the maze a statistically greater number of times as compared to WT mice, suggesting that they are less anxious and disinhibited. This is corrected by TMEM106B deficiency as *Grn*−/− *Tmem106b*−/− mice display normalized elevated plus maze behavior (Figure 8B). General locomotor behavior in the plus maze assay was not significantly different between the genotypes (data not shown). Taken together, these data show that in addition to rescuing the histological and biochemical abnormalities, *Tmem106b* deletion also rescues behavioral deficits in *Grn*−/− mice.

TMEM106B absence rescues retinal degeneration in *Grn*−/− mice

Previous studies have shown that *Grn*−/− mice develop retinal degeneration. Importantly, the retinal degenerative phenotype is also found in PGRN-deficient FTLD as well as NCL (Hafler et al., 2014; Ward et al., 2014). Our preliminary experiments show that the retinal degeneration can be detected in *Grn*−/− mice as early as 5 months of age (unpublished observations). We therefore tested whether TMEM106B deficiency modulates the retinal degeneration using 7-month-old animals. While immunostaining for Brn3a, a transcription factor expressed in most retinal ganglion cells (Nadal-Nicolas et al., 2009) shows a progressive degeneration of Brn3a-positive retinal ganglion cells in *Grn*−/− mice, there is no significant difference in the Brn3a-positive cells between WT, *Tmem106b*−/−, and *Grn*−/− *Tmem106b*−/− retinas (Figure 8C and 8D). As for brain, TMEM106B deficiency has no significant effect on lipofuscin accumulation in *Grn*−/− retina (Figure 8E and Figure S8A).

We also tested whether TMEM106B deficiency affects CD68-positive microglial accumulation in *Grn*−/− retina. We did not observe any significant change in CD68-positive immunoreactive area in *Grn*−/− *Tmem106b*−/− retina, compared to *Grn*−/− (Figure S8B and S8C). These results demonstrate that *Tmem106b* deletion also prevents retinal ganglion cell degeneration in *Grn*−/− mice despite the absence of rescue of lipofuscin and CD68-positive microglial accumulation.

DISCUSSION

The major finding of this study is that TMEM106B deficiency ameliorates not only lysosomal dysregulation but also FTLD-related behavioral and retinal degenerative phenotypes in *Grn*−/− mice. Importantly, accumulation of lipofuscin, CD68-positive microglia and complement C1q in *Grn*−/− mice is not reverted by TMEM106B loss. In addition, we found that TMEM106B physically interacts with V-ATPase and that loss of TMEM106B causes downregulation of V-ATPase V0 domain and impairment in lysosomal acidification, thereby normalizing the level of several lysosomal enzymes in *Grn*−/− neurons. Our findings provide novel insights into several important issues in the central nervous system.

The mechanism of PGRN deficiency-induced neurodegeneration

PGRN reduction is associated with several neurodegenerative disorders such as FTLD, NCL, and AD. Loss of the protein in mice affects diverse cellular processes especially at late stage of the animal lifetime (Kleinberger et al., 2013). In the present study, we therefore sought to understand the earliest changes that occur by PGRN deficiency. Our GO analysis using DE genes from transcriptomic and proteomic analyses of 2-month-old *Grn*−/− mice identified lysosome as the most significantly enriched terms, suggesting that lysosomal dysfunction is one of the earliest changes in *Grn*−/− mice.

Although our study is the most comprehensive study investigating the earliest changes in *Grn*−/− mice, previous studies have also examined transcriptomic change that occur as a result of PGRN deficiency. Rosen et al. utilized microarray transcriptome profiling of hNPCs with *GRN* knockdown, *GRN+* FTLD-TDP postmortem brain, and *Grn*−/− mice. The results of the study indicate that Wnt signaling is altered as a result of PGRN deficiency (Rosen et al., 2011). A recent study using transcriptome profiling using microarray of *Grn*−/− mice brain shows that the complement pathway is dysfunctional (Lui et al., 2016). These two studies differ from ours in key ways such as mouse lines, ages, and sequencing technique. However, interestingly, these studies have also identified upregulation of lysosomal genes, suggesting that lysosomal dysregulation is one of the most common events caused by PGRN deficiency. While Lui et al. investigated lysosomal defects in *Grn*−/− microglia, our DPPII and NeuN double immunostaining using the brain sections and lysosomal enzyme and proteolytic analyses using primary cultured neurons clearly suggest that lysosomal dysfunction occurs prominently in neurons. The mechanisms by which PGRN deficiency causes transcriptional and protein upregulation in lysosome is currently unclear and requires further investigation.

PGRN is also thought to be involved in microglial neuroinflammation. However, our RNASeq analysis showed no significant changes in pro- and anti-inflammatory genes and microglial markers such as iNOS, IL1β, TGFβ, Iba1 and CD11b in 2-month-old *Grn*−/− brain. We have also previously shown no significant changes in these genes at 6 months of age (Takahashi et al., 2017). On the other hand, consistent with a recent study (Lui et al., 2016), we found transcriptional upregulation of complement proteins including C1q as a part of microglial TNG in 2-month-old *Grn*−/− mice. The microglial TNG upregulation persists at 6 months of age (Takahashi et al., 2017). Remarkably, upregulation of TNG such as TYROBP (also known as DAP12 in mice), TREM2, MS4A7, CD68, and Lyz2 in *Grn*−/− mice has been observed in three independent transcriptome studies (Lui et al., 2016; Rosen et al., 2011; Takahashi et al., 2017).

Taken together, our study as well as previous transcriptome analyses using different *Grn*−/− strains suggests that upregulation in lysosomal genes and microglial TNG expression are most common changes caused by PGRN deficiency from the earliest stage. Microgliosis (increase in the number of Iba1-positive microglia) observed in several studies might occur as a result of these changes at later ages.

TMEM106B biology in the brain

Although there are several studies investigating TMEM106B biology, our study is the first to examine physiological role of *TMEM106B* in the brain *in vivo* using *Tmem106b*−/− mice. By using LFQ-LCMS and biochemical techniques, we report here that protein levels of several lysosomal enzymes including DPPII, CatB, and LAMP1 are decreased in *Tmem106b*−/− brain. These results clearly suggest that *TMEM106B* plays an important role in lysosomal homeostasis in the brain. Importantly, our study also shows that TMEM106B binds V-ATPase, an enzyme regulating lysosomal acidification, probably through V-ATPase AP1 and its deficiency causes downregulation of V-ATPase V0 domain subunits and AP1 and impairment in lysosomal acidification, thereby decreasing the lysosomal enzymes. Interestingly, previous *in vitro* studies have shown that overexpression of TMEM106B also exhibits impaired lysosomal acidification (Busch et al., 2016; Chen-Plotkin et al., 2012), although the underlying mechanisms are unclear. Similar results from overexpression and knockout experiments suggest that well-controlled balance of TMEM106B levels might be critical to maintain proper lysosomal acidification.

We have previously shown that overexpression of TMEM106B induces nuclear translocation of transcription factor EB (TFEB), a major regulator of lysosomal biogenesis and autophagy and upregulation of CLEAR network genes (Stagi et al., 2014). In the present study, our RNASeq analysis using 2-month-old *Tmem106b*−/− mice however showed only a minor transcriptional change (54 genes) and no lysosomal DE genes were identified except for *Tmem106b*. Quantitative real-time PCR using 7-month-old *Tmem106b*−/− mice also showed no significant changes in SLC17A5, CatD, CatS, and LAMP1, suggesting that TMEM106B deficiency has no significant effects on transcriptional change in lysosomal genes. The effect of TMEM106B on TFEB is apparently specific to overexpression. It is also possible that there are compensatory mechanisms upon constitutive TMEM106B deficiency.

The mechanism of *TMEM106B* modulation in PGRN-deficient FTLD-TDP

Accumulating evidence suggests that lysosomal dysregulation plays a role in FTLD as mutations in several endolysosomal genes have been found to cause FTLD, such as valosin containing protein (*VCP*) (Schroder et al., 2005; Watts et al., 2004), and charged multivesicular body 2B (*CHMP2B*) (Skibinski et al., 2005). Although *TMEM106B* has been linked to PGRN-deficient FTLD-TDP by genome-wide association studies and lysosomal localization of PGRN and TMEM106B is well established, the mechanisms by which *TMEM106B* modulates PGRN-deficient FTLD-TDP have been unclear. Importantly, it had been uncertain whether the TMEM106B gain- versus loss-of-function reduces PGRN-deficient FTLD risk. Our results reveal that *TMEM106B* controls lysosomal biology in an opposite fashion to *GRN.* We further observe that harnessing TMEM106B's opposing role in the lysosome by generating *Grn*−/− *Tmem106b*−/− mice leads to a reversal of the lysosomal phenotype seen in individual knockouts. The opposing actions on lysosomal biology by both of these FTLD-associated proteins may provide clues as to how *TMEM106B* modulates the PGRN-deficient FTLD phenotype in human patients. More specifically, our data suggest that the *TMEM106B* protective allele might cause loss-of-function of TMEM106B thereby reducing the FTLD risk. In addition, our study shows that loss of TMEM106B ameliorates FTLD-related phenotypes in *Grn*−/− mice without improving accumulation of CD68-positive microglia and complement C1q, suggesting that lysosomal dysfunction, rather than microglial and TNG changes, may play a central role in the pathogenesis of FTLD. This is also supported by our RNASeq analysis in *Tmem106b*−/− mice showing no significant changes in microglial genes.

In the present study, we found that while TMEM106B deficiency causes downregulation of V-ATPase V0 domain subunits, no significant changes in these subunits at both transcriptional and protein levels are found in *Grn*−/− mice. Therefore, lysosomal protein normalization that we observed in *Grn*−/− *Tmem106b*−/− mice is not simply due to correction of aberrant V-ATPase levels caused by PGRN deficiency. This is partially supported by the fact that TMEM106B deficiency does not normalize the dysregulation of all lysosomal enzymes observed in *Grn*−/− mice.

TDP-43-positive inclusions are a hallmark of PGRN-deficient FTLD-TDP. However, so far there are no studies that have successfully recapitulated the TDP-43 pathology using *Grn*−/− or *Grn*+/− mice. The mechanisms by which PGRN deficiency differentially affects TDP-43 pathology between humans versus mice are currently unclear and further investigation will be necessary.

The mechanism of lipofuscin formation and its role in neurodegeneration

Accelerated deposition of lipofuscin, autofluorescent lipopigment that accumulates in postmitotic cells over the lifetime of an organism, is frequently observed in neurodegenerative disorders including NCL and AD. A recent study has also reported increased lipofuscin in heterozygous *GRN* mutation carriers (Ward et al., 2017). The molecular mechanisms underlying increased lipofuscin accumulation by PGRN deficiency are currently unknown. In the present study, we found that TMEM106B deficiency has no significant effects on lipofuscin phenotype in *Grn*−/− mice despite rescue of dysfunction in

several lysosomal proteolytic enzymes. This result suggests that rescue of lipofuscin may require a broader or different correction of lysosomal enzymes in *Grn*−/− mice. Importantly, increased Hex A/B/S activity of *Grn*−/− mice is not affected by TMEM106B loss, suggesting that they are critical in lipofuscin accumulation in this strain. Further studies will be needed to clarify which lysosomal enzymes are involved in lipofuscin formation associated with PGRN loss. However, we have shown amelioration of retinal degeneration in *Grn*−/− *Tmem106b*−/− mice without improving lipofuscin phenotype. It remains controversial whether lipofuscin in the brain is pathogenic, inert, or protective (Gray and Woulfe, 2005; Stojanovic et al., 1994). Our findings suggest that lipofuscin may not be critical for neurodegeneration in FTLD and NCL.

In conclusion, our transcriptomic and proteomic analyses using *Grn*−/− and *Tmem106b*−/− mice uncovers the opposing role of these proteins in lysosomal enzyme homeostasis. In addition, amelioration of FTLD-related phenotypes in *Grn*−/− *Tmem106b*−/− mice suggests TMEM106B or V-ATPase inhibition as a potential therapeutic target for PGRN-deficient FTLD-TDP. It will be important to investigate whether impairment in lysosomal acidification by TMEM106B deficiency is also protective against the other contexts including *C9orf72*-related FTLD and AD.

STAR METHODS

CONTACT FOR REAGENT AND RESOURCE SHARING

Further information and requests for resources and reagents should be directed to and will be fulfilled by the Lead Contact, Stephen M. Strittmatter (stephen.strittmatter@yale.edu).

EXPERIMENTAL MODEL AND SUBJECT DETAILS

Mice—The targeting vector PGS00041_A_C06, developed by the Welcome Trust Sanger Institute, encoded an insertion of a *lacZ* gene trap cassette in between exons 3 and 4 of the *Tmem106b* gene. *Tmem106b*$^{tm1a(KOMP)Wtsi}$ mice were created by blastocyst injection of targeted ES-cell clone EPD0047_1_E02_M25 from the C57BL/6N strain from the Knockout Mouse Project (KOMP) Repository. *Grn*−/− mice, whose generation has been described previously (Kayasuga et al., 2007), were obtained from the RIKEN Bioresource Center. *Grn* −/− mice were on a C57BL/6J background. Age matched C57BL/6J mice were used as wild type controls. All mice were maintained on a 12 h light-dark schedule with access to standard mouse chow and water *ad libitum*. All animal studies were conducted with approval of the Yale Institutional Animal Care and Use Committee. Both male and female mice were included in all of these studies, with animals being collected from sequential littermates of the appropriate genotypes for various experiments. The age of mice was an experimental variable, and is specified in each Figure legend.

Primary Neuronal Culture—Primary mouse cortical neurons were prepared from E17-18 embryos (both male and female) as described previously (Hu et al., 2010), plated at 50,000 cells/well onto PDL-coated 96 well plates (CORNING #354461) and cultured in Neurobasal-A medium (Gibco) supplemented with B27, 1 mM sodium pyruvate,

GlutaMAX-I, and 100 U/mL penicillin and 100 μg/mL streptomycin (all from Gibco) at 37°C in 5% CO_2.

Cell culture and transfection—HEK293T cells (ATCC) were maintained in DMEM (Gibco) supplemented with 10% fetal bovine serum (Gibco), 100 U/mL penicillin and 100 μg/mL streptomycin (Gibco) at 37°C in 5% CO_2. Transient transfection was performed with Lipofectamine 2000 (Invitrogen).

METHOD DETAILS

Experimental Design—All behavioral measurements and all imaging quantifications were conducted by experimenters unaware of experimental group. Mice were collected sequentially from littermate cohorts without regard to sex or any characteristic other than the specified genotypes. The data from all observations were pooled by experimental group for statistical analysis. The n values are specified in each Figure legend, and reflect either separate mice or separate experimental batches as appropriate and as indicated. Sample sizes were determined to be comparable to previous studies that examined PGRN-related changes in CNS histology and behavior (Ahmed et al., 2010; Hafler et al., 2014; Takahashi et al., 2017; Yin et al., 2010a; Yin et al., 2010b).

RNASeq—RNA was extracted from cortex using Trizol extraction and Purelink® RNA kit (ThermoFisher Scientific). Bioanalyzer chips were used to assess RNA quality prior to RNA sequencing. 75 bp single-end sequencing was performed on an Illumina HiSeq 2000 machine (Illumina) following the manufacturer's instructions. Data quality was assessed using FastQC. Adaptor sequences were trimmed. Next, the first 6 bases from the 5′ region were trimmed. Bases with quality lower than 30 were removed from both ends. Any reads ≤ 45 bp after trimming were removed from further analysis. Reads that passed the quality control were aligned to the reference genome using TopHat2. The number of reads mapped to each transcript was obtained using HRSeq-count. Transcripts with ≥ to 1 read in at least 2 samples were kept for further analysis. Out of a total 39179 genes, 19489 genes were included at this step. Counts numbers were normalized using R package RUVseq to remove unwanted variations. Differential expression was tested for normalized count data using the R package edgeR, with a generalized linear model. Genes with FDR control p-value ≤ 0.05 were identified as differentially expressed genes. Heat maps were made using the matrix visualization and analysis platform, GENE-E (Broad Institute, http://www.broadinstitute.org/cancer/software/GENE-E/). STRING interactome software was used to visually represent the differentially expressed genes and perform Gene Ontology analysis (Jensen et al., 2009).

Mass spectrometry—Forebrains were washed briefly in ice cold PBS and blotted, homogenized in 4 volumes of 1x Extraction Buffer (Sigma, E1156) supplemented with Protease Inhibitor Cocktail (Sigma, P8340) in a dounce homogenizer. Lysates were centrifuged at 1,000 *x g* for 10 min at 4°C. The supernatant (supernatant 1) was removed and transferred to an empty tube. The pellet was then rehomogenized in 2 volumes of 1x Extraction Buffer and homogenized at 1,000 *x g* for 10 minutes at 4°C. The supernatant (supernatant 2) was pooled with supernatant 1 and centrifuged at 20,000 *x g* for 10 min at

4°C. The pellet was resuspended in RI PA (0.8 mL/g of original tissue) and spun down at 20,0000 *x g* for 10 min at 4°C and analyzed using mass spectrometry.

Chloroform-methanol:water protein precipitation was performed, and dried protein pellet was resuspended in Rapigest (Waters Inc) containing 50 mM ABC, reduced with DTT alkylated with iodoacetamide, and dual enzymatic digestion with LysC and trypsin (carried out at 37°C for 4 h), respectively. Digestion incubation was continued overnight (~16 h) and subsequently quenched (with 0.1% formic acid) during the de-salting step with C_{18} UltraMicroSpin columns. The effluents from the de-salting step were dried and re-dissolved in 5 µl 70% FA and 35 µl 0.1% TFA. An aliquot was taken to obtain total digested protein amount. A 1:10 dilution of Pierce Retention Time Calibration Mixture (Cat# 88321) was added to each sample prior to injecting on the UPLC LTQ Orbitrap ELITE mass spectrometer for normalization of LFQ data.

Label-Free Quantitation (LFQ) was performed on a Thermo Scientific Q-Exactive Plus mass spectrometer connected to a Waters nanoACQUITY UPLC system equipped with a Waters Symmetry® C18 180 µm × 20 mm trap column and a 1.7-µm, 75 µm × 250 mm nanoACQUITY UPLC column (35°C). The digests were diluted to 0. 05 µg/µl with 0.1% TFA prior to injecting 5 µl of each duplicate analysis in block randomized order. To ensure a high level of identification and quantitation integrity, a resolution of 60,000 was utilized for MS and 15 MS/MS spectra was acquired per MS scan using HCD. All MS (Profile) and MS/MS (centroid) peaks were detected in the Orbitrap. Trapping was carried out for 3 min at 5 µl/min in 99% Buffer A (0.1% FA in water) and 1% Buffer B [(0.075% FA in acetonitrile (ACN)] prior to eluting with linear gradients that will reach 30% B at 140 min, 40% B at 155 min, and 85% B at 160 min. Two blanks (1st 100% ACN, 2nd Buffer A) will follow each injection to ensure against sample carry over.

The LC-MS/MS data was processed with Progenesis QI Proteomics software (Nonlinear Dynamics, version 2.0) with protein identification carried out using the Mascot search algorithm. The Progenesis QI software performs feature/peptide extraction, chromatographic/spectral alignment (one run is chosen as a reference for alignment), data filtering, and quantitation of peptides and proteins. A normalization factor for each run was calculated to account for differences in sample load between injections as well as differences in ionization. The normalization factor was determined by comparing the abundance of the spike in Pierce Retention Time Calibration mixture among all the samples. The experimental design was setup to group multiple injections from each run. The algorithm then calculates the tabulated raw and normalized abundances, maximum fold change, and Anova p values for each feature in the data set. The MS/MS spectra was exported as .mgf (Mascot generic files) for database searching. The Mascot search results was exported as .xml files using a significance cutoff of $p < 0.05$ and FDR of 1% and then imported into the Progenesis QI software, where search hits was assigned to corresponding peptides. Relative protein-level fold changes were calculated from the sum of all unique, normalized peptide ion abundances for each protein in each run. Heat maps were made using the matrix visualization and analysis platform, GENE-E (Broad Institute, http://www.broadinstitute.org/cancer/software/GENE-E/). STRING interactome software was used to visually represent the differentially expressed proteins.

Brain homogenization and immunoblots—For immunoblot validation of mass spec hits, forebrains were homogenized in RIPA buffer supplemented with PhosSTOP™ and 1 × cOmplete™ Mini protease inhibitor cocktail (Roche) to measure protein expression. The protein concentration in the RIPA soluble fraction was determined by Bradford assay (Bio-Rad Protein Assay). The RIPA soluble fraction was then mixed with SDS-PAGE sample loading buffer and proteins were resolved by SDS-PAGE followed by immunoblot. Proteins were electrophoresed through precast 4–20% Tris-glycine gels (Bio-Rad) and transferred with an iBlot™ Gel Transfer Device (Novex-Life Technologies) onto nitrocellulose membranes (Invitrogen). Membranes were incubated in blocking buffer (Rockland, MB-070-010) for 1 h at RT. Membranes were then washed three times in TBST, and incubated overnight in primary antibodies. The following primary antibodies were used: rat anti-LAMP1 (Santa Cruz, 1D4B, sc-19992), goat anti-mouse Cathepsin B (R&D Systems, AF965, 1:500), goat anti-mouse Cathepsin L (R&D Systems, AF1515, 1:500), goat anti-mouse DPPII (R&D Systems, AF3436, 1:500), and mouse anti-β-actin (8H10D10) (Cell Signaling Technology, #3700, 1:2500). All antibodies were diluted in blocking buffer, and membranes were incubated overnight at 4°C. Following primary antibody incubation, the membranes were washed three times with TBST, and secondary antibodies were applied for 1 h at RT (Li-Cor Biosciences, 1:10 000 donkey anti-mouse, donkey anti-rabbit, donkey anti-rat, and donkey anti-goat, IRDye 680 or 800). Membranes were then washed and proteins visualized using an Odyssey Infrared imaging system (Li-Cor Biosciences). Immunoreactive bands were quantified using the Li-Cor Odyssey software.

Lysosomal enzyme activity assay—Forebrains or primary cultured neurons (DIV 21) from WT, *Grn*−/−, *Tmem106b*−/−, and *Grn*−/− *Tmeme106b*−/− mice were homogenized in 50 mM Tris-HCl pH 7.4, 150 mM NaCl, 1% Trion X-100 without protease inhibitors. After ultracentrifugation at 100,000 x *g* for 20 min, the supernatants were immediately snap-frozen for the enzyme activity assays. Cat B activity assay (EMD Millipore, CBA001) was performed according to the manufacturer's protocols using 100 μg brain lysate. DPPII activity assay was performed using fluorogenic substrate H-Lys-Ala-AMC (Bachem, I-1260) and DPPII inhibitor UAMC00039 (Tocris, 4954). Briefly, brain lysates or neuronal lysates (10 μg) and 100 μM H-Lys-Ala-AMC were diluted into 100 μL of 50 mM MES buffer pH 6 in the presence or absence of 20 μM UAMC00039 and incubated for 30 min (brain lysates) or 2 h (neuronal lysates) at 37°C. TPP1 activity was performed using fluorogenic substrate H-Ala-Ala-Phe-AMC (Bachem, I-1415). Briefly, neuronal lysates (15 μg) and 250 μM H-Ala-Ala-Phe-AMC were diluted into 100 μL of 10 mM citrate buffer pH 4.2 and incubated for 2 h at 37°C. Hex A/B/S activity assay was performed as previously reported with slight modification (Tropak et al., 2004). Briefly, brain lysates (0.5 μg) and 2.5 mM Hex A/B/S substrate 4-Methylumbellifery N-acetyl-β-D-glucosaminide (Sigma, M2133) were diluted in 50 μL of 10 mM citrate buffer pH 4.2 and incubated for 1 h at 37°C. For Hex A/B/S assay, the reaction was stopped by adding 200 μL of 0.1 M 2-Amino-2-methyl-1-propanol (Sigma, 08578) pH 11. Fluorescence (ex 355 nm, em 440–460 nm) was measured in Victor 3V plate reader (Perkin Elmer). For Cat B and DPPII assays, the fluorescence value of all samples was corrected by subtracting the value of the samples assayed with the inhibitor. An AMC (7-Amino-4-methylcoumarin) standard (EMD Millipore, CBA001) for Cat B, DPPII, and TPP1 assays and a 4-MU (4-Methylumbelliferone) standard (Sigma M1381) for Hex A/B/S

assay were used to calculate the amount (nmol) of free AMC or 4-MU per mg of total protein and time unit.

Protein degradation measurement—Protein degradation rates were measured as previously described (Kaushik and Cuervo, 2009) with a slight modification. Briefly, primary cultured neurons were prepared from E17-18 WT, *Grn*−/−, *Tmem*−/−, and *Grn*−/− *Tmem*−/− embryo as reported (Hu et al., 2010) and plated onto PDL-coated 96 well plates (50,000 cells/well). On DIV 19, neurons were labeled with 2.5 μCi/mL [^{3}H]-leucine for 48 h at 37°C. On DIV 21, the neurons were washed with conditioned medium supplemented with 2.8 mM unlabeled leucine 2 times for 10 min, followed by 1 time for 2 h to remove free amino acids from short-lived proteins. After washing, the neurons were incubated in fresh neurobasal medium supplemented with 2.8 mM unlabeled leucine in the presence or absence of 50 μM leupeptin and 20 mM NH_4Cl for 8 h at 37°C. Aliquots of the medium were taken at 0 h and 8 h incubation and precipitated with 0.5 mg/mL BSA and 10% TCA. After centrifugation at 20,000 x *g* for 20 min at 4°C, the supernatants were collected and the pellets were dissolved in 0.1M NaOH, 0.1% sodium deoxycholate. The neurons were washed once with neurobasal medium and solubilized in 0.1 NaOH, 0.1% sodium deoxycholate. The radioactivity was measured in scintillation cocktail using liquid scintillation counter (Beckman). Percent proteolysis was calculated as described previously (Kaushik and Cuervo, 2009).

Immunohistochemistry—Animals were rapidly euthanized and brains were immediately post-fixed in 4% PFA for 24 h at 4°C. Brains were then sliced on a vibratome (Leica) and collected as 40 μm free-floating sections. Sections were collected in PBS. Sections were blocked with 10% fish serum (Aves), 0.1% Triton X-100 in PBS for 1 h, followed by incubation with primary antibody overnight at 4°C. Primary antibodies were diluted in fish serum (1:100), 0.1% Triton X-100 in PBS. The following primary antibodies were used: rat anti-mouse CD68 (AbD Serotec, MCA1957, 1:1000), goat anti-mouse DPPII (R&D Systems, AF3436, 1:500), mouse anti-NeuN (Millipore MAB377), rabbit monoclonal anti-C1q [4.8] (abcam, ab182451, 1:1000). The sections were washed three times with PBS, incubated in secondary fluorescent antibody (Invitrogen Alexa Fluor, all 1:500) for 2 h. In order to quench autofluorescence, the sections were treated with 10 mM $CuSO_4$ in ammonium acetate for 15 min (Schnell et al., 1999). Images of three sections from each animal were captured using LSM710 confocal microscopy with a 63× objective lens (for DPPII) or Zeiss AxioImager Z1 epifluorescent microscopy with a 5× objective lens (for CD68 and C1q). For the CD68 and C1q cortical analysis, the cortex area dorsal to the hippocampus was assessed. DPPII images were analyzed using ImageJ software with a single automated macro script to quantitate areas. C1q and CD68 images were analyzed as previously reported using ImageJ (Takahashi et al., 2017). All analyses were performed without knowledge of genotype.

Autofluorescence—Brains were collected and processed as described above. After washing in PBS, autofluorescence was visualized on Zeiss AxioImager Z1 epifluorescent microscope with multiple excitation wavelengths including 488 nm and 543 nm. Brains were

photographed using a 20x Plan objective lens. Three sections per animal were analyzed as for immunohistology.

LysoTracker Red DND-99 staining—Primary cultured neurons were prepared from E17-18 WT and *Tmem106b*−/− embryo as previously reported (Hu et al., 2010) and plated onto PDL-coated 96 well plates (50,000 cells/well). On DIV 21–24, neurons were stained with LysoTracker Red DND-99 (Invitrogen, L7528, 100 nM) for 10 min, washed once with neurobasal media, and then immediately imaged. MAP2 staining was performed with the same batch of neurons on PDL-coated 96 well plates prepared for LysoTracker staining. Neurons were fixed with 4% PFA for 30 min and blocked with 10% normal donkey serum, 0.2% Triton X-100 in PBS for 30 min, followed by incubation with primary antibody overnight at 4°C. Anti-MAP2 a ntibody (Millipore, MAB3418, 1:200) was diluted in 1% normal donkey serum, 0.2% Triton X-100 in PBS. The samples were washed three times with PBS and incubated in Alexa Fluor 488 donkey anti-mouse antibody (Invitrogen, A21202, 1:500) for 1 h. Images of LysoTracker and MAP2 staining were automatically taken using ImageXpress Micro XLS (Molecular Devices) (40X objective lens). LysoTracker-positive area, mean fluorescence intensity, and integrated fluorescence intensity and MAP2-positive areas were analyzed using ImageJ 1.47v software (National Institutes of Health). All images were uniformly thresholded for the LysoTracker- or MAP2-positive area analysis.

Co-immunoprecipitation assay—GFP, mCherry, TMEM106B-GFP, and TMEM106B-mCherry plasmids were described previously (Stagi et al., 2014). Deletion mutants of TMEM106B-GFP lacking 6–94 aa and 123–275 aa were made using Quik Change Mutagenesis (Agilent Genomics) and subcloning, respectively. All constructs were verified by sequencing. Myc-DDK-tagged protein plasmids (V-ATPase V0c, V0d1, and AP1, and CatB) were obtained from OriGene Technologies, Inc. Two days after transient transfection, HEK293T cells expressing GFP or TMEM106B-GFP or mCherry or TMEM106B-mCherry, together with myc-DDK-tagged proteins were lysed with ice-cold 50 mM Tris-HCl, pH 7.4, 150 mM NaCl, 0.5 mM EDTA, 0.5% NP-40 supplemented with cOmplete™ Mini (Roche). After ultracentrifugation at 100,000 x g, the supernatant was incubated with GFP-trap or RFP-trap (Chromotek) for 3 h at 4°C. The immunoprecipitates were washed at least four times with ice-cold 50 mM Tris-HCl, pH 7.4, 150 mM NaCl, 0.5 mM EDTA, 0.05% NP-40 and boiled with 2 x SDS sample buffer with βME.

Retinal cell count determination—Retinas were collected at 7 months of age and processed as described in (Hafler et al., 2014). Briefly, after dissection, retinas were post-fixed for 1–3 h after dissection. Following fixation, retinas were cryoprotected in 30% sucrose PBS solution overnight at 4°C. After cryoprotection, retinas were embedded using OCT and rapidly frozen on dry ice. 20 μm sections were sliced on a cryostat and collected immediately on microscope slides. Retinas were then stained on slides. Primary antibody was applied overnight at 4°C. Primary antibody used was rabbit anti-Brn3a (Santa Cruz, H-80 sc-28595, 1:250). The secondary antibody used was Alexa Fluor® 568-conjugated donkey anti-rabbit IgG (Invitrogen, A10042, 1:500). Vectashield mounting media with DAPI (Vectorlabs, H-1200) was used to stain nuclei. After washing in PBS, fluorescent stains were

visualized on Zeiss AxioImager Z1 fluorescent microscope with a 10x air objective. Within the ganglion cell layer, the number of immunostained Brn3a cells was counted per 500 μm for each retinal section from the central regions. Data was averaged from 4–8 slices of each retina. At least three independent retinas were quantified for each experiment, and all counts were made by an observed unaware of the genotypes.

Elevated plus maze—Elevated plus maze was set at a height of 65 cm and consisted of two open white Plexiglas arms, each arm 8 cm wide x 30 cm long and two enclosed arms (30 cm x 5 cm) with 15 cm high walls which were connected by a central platform (5 cm x 5 cm). Individual mice were placed at the center of the maze and were observed for 5 min. All arms were cleaned with 70% ethanol after every trial. Male and female mice (gender-matched across groups) were tested at 4 months of age.

Open field test—The apparatus for the open field test consisted of a grey, 50-cm-wide × 50-cm-long × 40-cm-high acrylamide box, with an open top. Individual mice were placed in the center of the box, and the total distance traveled analyzed by computer with the program described above. The apparatus was cleaned with 70% ethanol after every trial. Male and female mice (gender-matched across groups) were tested at 4 months of age.

Behavior analysis—Elevated plus maze and open field behavior was recorded on a JVC (Yokohama, Japan) Everio G-series camcorder and tracked by Panlab (Barcelona, Spain) Smart software. All behavioral experiments were conducted by personnel unaware of the genotypes.

Quantitative real-time PCR—RNA was extracted from cortex using Trizol extraction and Purelink® RNA kit (ThermoFisher Scientific). RNA was reverse-transcribed using the Bio-rad iScript cDNA Synthesis Kit or the SuperScript III first-strand synthesis system (ThermoFisher Scientific) according to the manufacturer's instructions. Samples were prepared using iQ or iTaq Universal Supermix (Bio-Rad). Taqman Primer-probe for Tmem106b (Mm00510952_m1) was used along with an Actin control. For the other genes, mRNA expression values were normalized to the level of GAPDH expression. The following probes from Thermo Fisher Scientific were used: GAPDH (Mm99999915_g1), SLC17A5 (Mm00555344_m1), CatD (Mm00515586_m1), CatS (Mm01255859_m1), LAMP1 (Mm00495262_m1), C1qA (Mm00432142_m1), C1qB (Mm01179619_m1). Quantitative real-time PCR was performed using the C1000 Thermal Cycler and quantified using the CFX96 Real-Time System (Bio-Rad).

QUANTIFICATION AND STATISTICAL ANALYSIS

Two-tailed unpaired T-test (for 2 groups) and one-way ANOVA (for > 3 groups) were performed using GraphPad Prism (version 5.0d). Gaussian distributions were assumed based on previous studies with behavior tests and our preliminary experiments. All data are shown as mean ± sem and specific n values are reported in each Figure legend. Data are considered to be statistically significant if $p < 0.05$.

DATA AND SOFTWARE AVAILABILITY

Detailed datasets from the RNAseq and Mass Spectrometry are provided in the Supplemental Tables.

Supplementary Material

Refer to Web version on PubMed Central for supplementary material.

Acknowledgments

We thank Stefano Sodi for assistance with mouse husbandry and Susumu Tomita with [3H]leucine metabolic labeling. We also thank the Yale School of Medicine for funding the Q-Exactive Plus LC MS/MS system located within the Yale MS & Proteomics Resource of the WM Keck Foundation Biotechnology Resource Laboratory; and Edward Voss, Jean Kanyo, and Kathrin Wilczak for helping with MS sample preparation, data collection, and analysis, respectively. This work was supported by grants from NIH and the Falk Medical Research Trust to S.M.S.

References

Ahmed Z, Sheng H, Xu YF, Lin WL, Innes AE, Gass J, Yu X, Wuertzer CA, Hou H, Chiba S, et al. Accelerated lipofuscinosis and ubiquitination in granulin knockout mice suggest a role for progranulin in successful aging. Am J Pathol. 2010; 177:311–324. [PubMed: 20522652]

Brady OA, Zheng Y, Murphy K, Huang M, Hu F. The frontotemporal lobar degeneration risk factor, TMEM106B, regulates lysosomal morphology and function. Human molecular genetics. 2013; 22:685–695. [PubMed: 23136129]

Busch JI, Unger TL, Jain N, Tyler Skrinak R, Charan RA, Chen-Plotkin AS. Increased expression of the frontotemporal dementia risk factor TMEM106B causes C9orf72-dependent alterations in lysosomes. Hum Mol Genet. 2016; 25:2681–2697. [PubMed: 27126638]

Cenik B, Sephton CF, Kutluk Cenik B, Herz J, Yu G. Progranulin: a proteolytically processed protein at the crossroads of inflammation and neurodegeneration. J Biol Chem. 2012; 287:32298–32306. [PubMed: 22859297]

Chen-Plotkin AS, Unger TL, Gallagher MD, Bill E, Kwong LK, Volpicelli-Daley L, Busch JI, Akle S, Grossman M, Van Deerlin V, et al. TMEM106B, the risk gene for frontotemporal dementia, is regulated by the microRNA-132/212 cluster and affects progranulin pathways. J Neurosci. 2012; 32:11213–11227. [PubMed: 22895706]

Colacurcio DJ, Nixon RA. Disorders of lysosomal acidification-The emerging role of v-ATPase in aging and neurodegenerative disease. Ageing research reviews. 2016; 32:75–88. [PubMed: 27197071]

Cotter K, Stransky L, McGuire C, Forgac M. Recent Insights into the Structure, Regulation, and Function of the V-ATPases. Trends Biochem Sci. 2015; 40:611–622. [PubMed: 26410601]

Cruchaga C, Graff C, Chiang HH, Wang J, Hinrichs AL, Spiegel N, Bertelsen S, Mayo K, Norton JB, Morris JC, et al. Association of TMEM106B gene polymorphism with age at onset in granulin mutation carriers and plasma granulin protein levels. Archives of neurology. 2011; 68:581–586. [PubMed: 21220649]

De Muynck L, Van Damme P. Cellular effects of progranulin in health and disease. J Mol Neurosci. 2011; 45:549–560. [PubMed: 21611805]

de Vugt ME, Riedijk SR, Aalten P, Tibben A, van Swieten JC, Verhey FR. Impact of behavioural problems on spousal caregivers: a comparison between Alzheimer's disease and frontotemporal dementia. Dement Geriatr Cogn Disord. 2006; 22:35–41. [PubMed: 16679763]

Dickson DW, Baker M, Rademakers R. Common Variant in GRN Is a Genetic Risk Factor for Hippocampal Sclerosis in the Elderly. Neurodegener Dis. 2010; 7:170–174. [PubMed: 20197700]

Filiano AJ, Martens LH, Young AH, Warmus BA, Zhou P, Diaz-Ramirez G, Jiao J, Zhang Z, Huang EJ, Gao FB, et al. Dissociation of frontotemporal dementia-related deficits and neuroinflammation in progranulin haploinsufficient mice. J Neurosci. 2013; 33:5352–5361. [PubMed: 23516300]

Finch N, Carrasquillo MM, Baker M, Rutherford NJ, Coppola G, Dejesus-Hernandez M, Crook R, Hunter T, Ghidoni R, Benussi L, et al. TMEM106B regulates progranulin levels and the penetrance of FTLD in GRN mutation carriers. Neurology. 2011; 76:467–474. [PubMed: 21178100]

Forgac M. Vacuolar ATPases: rotary proton pumps in physiology and pathophysiology. Nat Rev Mol Cell Biol. 2007; 8:917–929. [PubMed: 17912264]

Gallagher MD, Suh E, Grossman M, Elman L, McCluskey L, Van Swieten JC, Al-Sarraj S, Neumann M, Gelpi E, Ghetti B, et al. TMEM106B is a genetic modifier of frontotemporal lobar degeneration with C9orf72 hexanucleotide repeat expansions. Acta Neuropathol. 2014; 127:407–418. [PubMed: 24442578]

Gotzl JK, Mori K, Damme M, Fellerer K, Tahirovic S, Kleinberger G, Janssens J, van der Zee J, Lang CM, Kremmer E, et al. Common pathobiochemical hallmarks of progranulin-associated frontotemporal lobar degeneration and neuronal ceroid lipofuscinosis. Acta neuropathologica. 2014; 127:845–860. [PubMed: 24619111]

Gray DA, Woulfe J. Lipofuscin and aging: a matter of toxic waste. Science of aging knowledge environment: SAGE KE. 2005; 2005:re1. [PubMed: 15689603]

Hafler BP, Klein ZA, Jimmy Zhou Z, Strittmatter SM. Progressive retinal degeneration and accumulation of autofluorescent lipopigments in Progranulin deficient mice. Brain Res. 2014; 1588:168–174. [PubMed: 25234724]

Hu F, Padukkavidana T, Vaegter CB, Brady OA, Zheng Y, Mackenzie IR, Feldman HH, Nykjaer A, Strittmatter SM. Sortilin-mediated endocytosis determines levels of the frontotemporal dementia protein, progranulin. Neuron. 2010; 68:654–667. [PubMed: 21092856]

Jensen LJ, Kuhn M, Stark M, Chaffron S, Creevey C, Muller J, Doerks T, Julien P, Roth A, Simonovic M, et al. STRING 8--a global view on proteins and their functional interactions in 630 organisms. Nucleic Acids Res. 2009; 37:D412–416. [PubMed: 18940858]

Jian J, Tian QY, Hettinghouse A, Zhao S, Liu H, Wei J, Grunig G, Zhang W, Setchell KD, Sun Y, et al. Progranulin Recruits HSP70 to beta-Glucocerebrosidase and Is Therapeutic Against Gaucher Disease. Ebiomedicine. 2016a; 13:212–224. [PubMed: 27789271]

Jian J, Zhao S, Tian QY, Liu H, Zhao Y, Chen WC, Grunig G, Torres PA, Wang BC, Zeng B, et al. Association Between Progranulin and Gaucher Disease. Ebiomedicine. 2016b; 11:127–137. [PubMed: 27515686]

Jing H, Tan MS, Yu JT, Tan L. The Role of PGRN in Alzheimer's Disease. Mol Neurobiol. 2016; 53:4189–4196. [PubMed: 26215834]

Kaushik S, Cuervo AM. Methods to monitor chaperone-mediated autophagy. Methods in enzymology. 2009; 452:297–324. [PubMed: 19200890]

Kayasuga Y, Chiba S, Suzuki M, Kikusui T, Matsuwaki T, Yamanouchi K, Kotaki H, Horai R, Iwakura Y, Nishihara M. Alteration of behavioural phenotype in mice by targeted disruption of the progranulin gene. Behavioural brain research. 2007; 185:110–118. [PubMed: 17764761]

Kleinberger G, Capell A, Haass C, Van Broeckhoven C. Mechanisms of granulin deficiency: lessons from cellular and animal models. Mol Neurobiol. 2013; 47:337–360. [PubMed: 23239020]

Lang CM, Fellerer K, Schwenk BM, Kuhn PH, Kremmer E, Edbauer D, Capell A, Haass C. Membrane orientation and subcellular localization of transmembrane protein 106B (TMEM106B), a major risk factor for frontotemporal lobar degeneration. The Journal of biological chemistry. 2012; 287:19355–19365. [PubMed: 22511793]

Lui H, Zhang J, Makinson SR, Cahill MK, Kelley KW, Huang HY, Shang Y, Oldham MC, Martens LH, Gao F, et al. Progranulin Deficiency Promotes Circuit-Specific Synaptic Pruning by Microglia via Complement Activation. Cell. 2016; 165:921–935. [PubMed: 27114033]

Mindell JA. Lysosomal acidification mechanisms. Annu Rev Physiol. 2012; 74:69–86. [PubMed: 22335796]

Murray ME, Cannon A, Graff-Radford NR, Liesinger AM, Rutherford NJ, Ross OA, Duara R, Carrasquillo MM, Rademakers R, Dickson DW. Differential clinicopathologic and genetic features of late-onset amnestic dementias. Acta Neuropathol. 2014; 128:411–421. [PubMed: 24899141]

Nadal-Nicolas FM, Jimenez-Lopez M, Sobrado-Calvo P, Nieto-Lopez L, Canovas-Martinez I, Salinas-Navarro M, Vidal-Sanz M, Agudo M. Brn3a as a marker of retinal ganglion cells: qualitative and

quantitative time course studies in naive and optic nerve-injured retinas. Investigative ophthalmology & visual science. 2009; 50:3860–3868. [PubMed: 19264888]

Nelson PT, Wang WX, Partch AB, Monsell SE, Valladares O, Ellingson SR, Wilfred BR, Naj AC, Wang LS, Kukull WA, et al. Reassessment of risk genotypes (GRN, TMEM106B, and ABCC9 variants) associated with hippocampal sclerosis of aging pathology. J Neuropathol Exp Neurol. 2015; 74:75–84. [PubMed: 25470345]

Nicholson AM, Rademakers R. What we know about TMEM106B in neurodegeneration. Acta Neuropathol. 2016; 132:639–651. [PubMed: 27543298]

Petkau TL, Leavitt BR. Progranulin in neurodegenerative disease. Trends Neurosci. 2014; 37:388–398. [PubMed: 24800652]

Petkau TL, Neal SJ, Milnerwood A, Mew A, Hill AM, Orban P, Gregg J, Lu G, Feldman HH, Mackenzie IR, et al. Synaptic dysfunction in progranulin-deficient mice. Neurobiol Dis. 2012; 45:711–722. [PubMed: 22062772]

Rosen EY, Wexler EM, Versano R, Coppola G, Gao F, Winden KD, Oldham MC, Martens LH, Zhou P, Farese RV Jr, et al. Functional genomic analyses identify pathways dysregulated by progranulin deficiency, implicating Wnt signaling. Neuron. 2011; 71:1030–1042. [PubMed: 21943601]

Rutherford NJ, Carrasquillo MM, Li M, Bisceglio G, Menke J, Josephs KA, Parisi JE, Petersen RC, Graff-Radford NR, Younkin SG, et al. TMEM106B risk variant is implicated in the pathologic presentation of Alzheimer disease. Neurology. 2012; 79:717–718. [PubMed: 22855871]

Schnell SA, Staines WA, Wessendorf MW. Reduction of lipofuscin-like autofluorescence in fluorescently labeled tissue. J Histochem Cytochem. 1999; 47:719–730. [PubMed: 10330448]

Schroder R, Watts GD, Mehta SG, Evert BO, Broich P, Fliessbach K, Pauls K, Hans VH, Kimonis V, Thal DR. Mutant valosin-containing protein causes a novel type of frontotemporal dementia. Annals of neurology. 2005; 57:457–461. [PubMed: 15732117]

Schwenk BM, Lang CM, Hogl S, Tahirovic S, Orozco D, Rentzsch K, Lichtenthaler SF, Hoogenraad CC, Capell A, Haass C, et al. The FTLD risk factor TMEM106B and MAP6 control dendritic trafficking of lysosomes. EMBO J. 2014; 33:450–467. [PubMed: 24357581]

Skibinski G, Parkinson NJ, Brown JM, Chakrabarti L, Lloyd SL, Hummerich H, Nielsen JE, Hodges JR, Spillantini MG, Thusgaard T, et al. Mutations in the endosomal ESCRTIII-complex subunit CHMP2B in frontotemporal dementia. Nat Genet. 2005; 37:806–808. [PubMed: 16041373]

Smith KR, Damiano J, Franceschetti S, Carpenter S, Canafoglia L, Morbin M, Rossi G, Pareyson D, Mole SE, Staropoli JF, et al. Strikingly different clinicopathological phenotypes determined by progranulin-mutation dosage. Am J Hum Genet. 2012; 90:1102–1107. [PubMed: 22608501]

Stagi M, Klein ZA, Gould TJ, Bewersdorf J, Strittmatter SM. Lysosome size, motility and stress response regulated by fronto-temporal dementia modifier TMEM106B. Mol Cell Neurosci. 2014; 61:226–240. [PubMed: 25066864]

Stojanovic A, Roher AE, Ball MJ. Quantitative analysis of lipofuscin and neurofibrillary tangles in the hippocampal neurons of Alzheimer disease brains. Dementia. 1994; 5:229–233. [PubMed: 7951677]

Takahashi H, Klein ZA, Bhagat SM, Kaufman AC, Kostylev MA, Ikezu T, Strittmatter SM. Alzheimer's Disease Neuroimaging, I. Opposing effects of progranulin deficiency on amyloid and tau pathologies via microglial TYROBP network. Acta neuropathologica. 2017; 133:785–807. [PubMed: 28070672]

Toei M, Saum R, Forgac M. Regulation and isoform function of the V-ATPases. Biochemistry. 2010; 49:4715–4723. [PubMed: 20450191]

Tropak MB, Reid SP, Guiral M, Withers SG, Mahuran D. Pharmacological enhancement of beta-hexosaminidase activity in fibroblasts from adult Tay-Sachs and Sandhoff Patients. J Biol Chem. 2004; 279:13478–13487. [PubMed: 14724290]

van Blitterswijk M, Mullen B, Nicholson AM, Bieniek KF, Heckman MG, Baker MC, DeJesus-Hernandez M, Finch NA, Brown PH, Murray ME, et al. TMEM106B protects C9ORF72 expansion carriers against frontotemporal dementia. Acta Neuropathol. 2014; 127:397–406. [PubMed: 24385136]

Van Deerlin VM, Sleiman PM, Martinez-Lage M, Chen-Plotkin A, Wang LS, Graff-Radford NR, Dickson DW, Rademakers R, Boeve BF, Grossman M, et al. Common variants at 7p21 are

associated with frontotemporal lobar degeneration with TDP-43 inclusions. Nat Genet. 2010; 42:234–239. [PubMed: 20154673]

von Mering C, Huynen M, Jaeggi D, Schmidt S, Bork P, Snel B. STRING: a database of predicted functional associations between proteins. Nucleic Acids Res. 2003; 31:258–261. [PubMed: 12519996]

Ward ME, Chen R, Huang HY, Ludwig C, Telpoukhovskaia M, Taubes A, Boudin H, Minami SS, Reichert M, Albrecht P, et al. Individuals with progranulin haploinsufficiency exhibit features of neuronal ceroid lipofuscinosis. Science translational medicine. 2017; 9

Ward ME, Taubes A, Chen R, Miller BL, Sephton CF, Gelfand JM, Minami S, Boscardin J, Martens LH, Seeley WW, et al. Early retinal neurodegeneration and impaired Ran-mediated nuclear import of TDP-43 in progranulin-deficient FTLD. The Journal of experimental medicine. 2014; 211:1937–1945. [PubMed: 25155018]

Watts GD, Wymer J, Kovach MJ, Mehta SG, Mumm S, Darvish D, Pestronk A, Whyte MP, Kimonis VE. Inclusion body myopathy associated with Paget disease of bone and frontotemporal dementia is caused by mutant valosin-containing protein. Nat Genet. 2004; 36:377–381. [PubMed: 15034582]

Yin F, Banerjee R, Thomas B, Zhou P, Qian L, Jia T, Ma X, Ma Y, Iadecola C, Beal MF, et al. Exaggerated inflammation, impaired host defense, and neuropathology in progranulin-deficient mice. J Exp Med. 2010a; 207:117–128. [PubMed: 20026663]

Yin F, Dumont M, Banerjee R, Ma Y, Li H, Lin MT, Beal MF, Nathan C, Thomas B, Ding A. Behavioral deficits and progressive neuropathology in progranulin-deficient mice: a mouse model of frontotemporal dementia. FASEB journal: official publication of the Federation of American Societies for Experimental Biology. 2010b; 24:4639–4647. [PubMed: 20667979]

Yoshimori T, Yamamoto A, Moriyama Y, Futai M, Tashiro Y. Bafilomycin A1, a specific inhibitor of vacuolar-type H(+)-ATPase, inhibits acidification and protein degradation in lysosomes of cultured cells. J Biol Chem. 1991; 266:17707–17712. [PubMed: 1832676]

Zhang J, Feng Y, Forgac M. Proton conduction and bafilomycin binding by the V0 domain of the coated vesicle V-ATPase. J Biol Chem. 1994; 269:23518–23523. [PubMed: 8089118]

Zhou X, Sun L, Bastos de Oliveira F, Qi X, Brown WJ, Smolka MB, Sun Y, Hu F. Prosaposin facilitates sortilin-independent lysosomal trafficking of progranulin. J Cell Biol. 2015; 210:991–1002. [PubMed: 26370502]

HIGHLIGHTS

- Transcriptomic and proteomic evidence of lysosomal dysregulation in *Grn*−/− mice
- *Tmem106b*−/− mice show opposite protein changes in lysosomes
- TMEM106B interacts with V-ATPase and regulates lysosomal acidification
- TMEM106B deficiency rescues lysosomal, behavioral and degenerative *Grn* −/−phenotypes

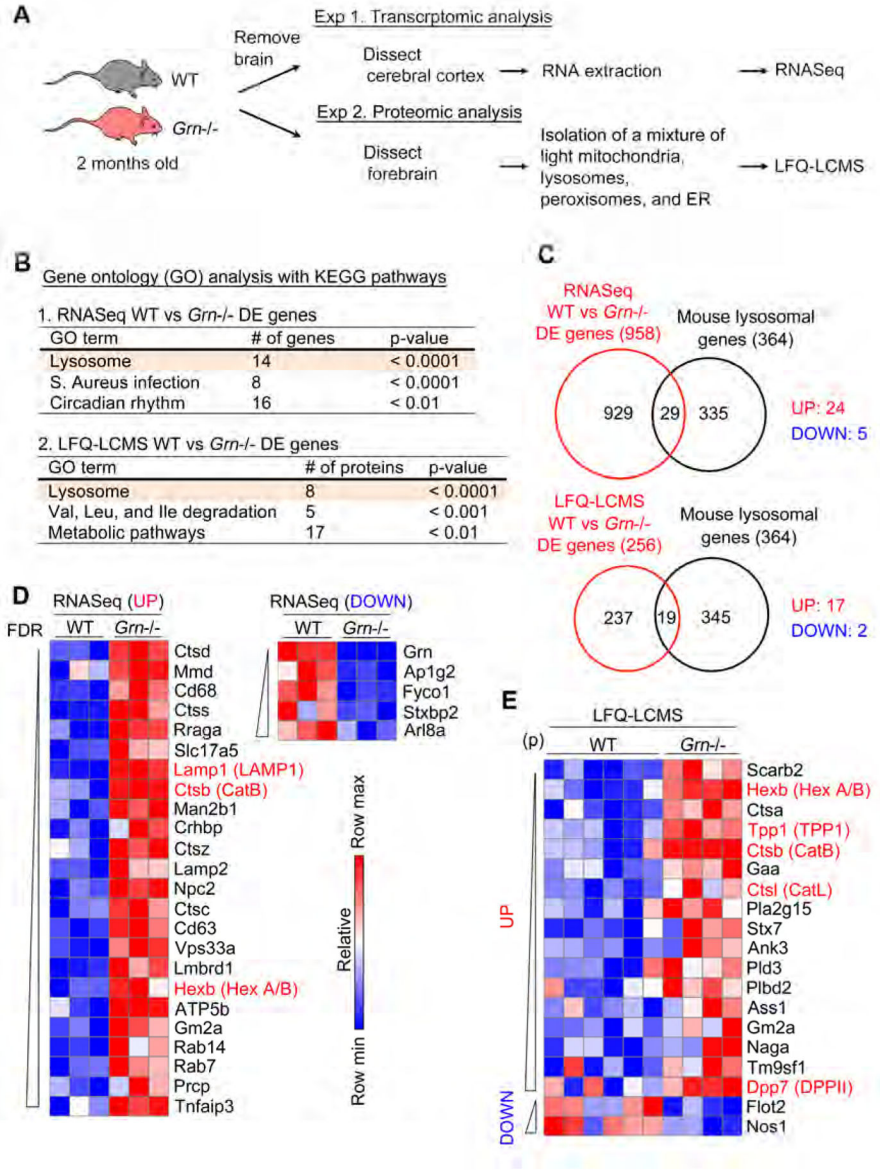

Figure 1. Transcriptomics and proteomics analyses reveal global changes in the lysosomal pathway in *Grn−/−* mice

(A) Diagram showing the experimental procedures of transcriptomic and proteomic analyses using WT and *Grn−/−* animals.

(B) Gene Ontology (GO) analysis of RNASeq and LFQ-LCMS dataset using KEGG pathways featuring the 3 pathways that reached significance ($p < 0.05$ after Bonferroni correction). Lysosome is most significantly enriched pathway in both datasets.

(C) Venn diagrams showing the overlap between differentially expressed (DE) genes identified by RNASeq or LFQ-LCMS and mouse lysosomal genes.

(D) Heatmap from Gene-E showing the common 24 upregulated and 5 downregulated genes identified in (C) using RNASeq dataset ($P < 0.05$ FDR, ranked by p value). Relative scale is represented below. Data are row-normalized.

(E) Heatmap from Gene-E showing the common 17 upregulated and 2 downregulated genes identified in (C) using LFQ-LCMS dataset ($P < 0.05$, ranked by p value). Relative scale is represented below. Data are row-normalized.

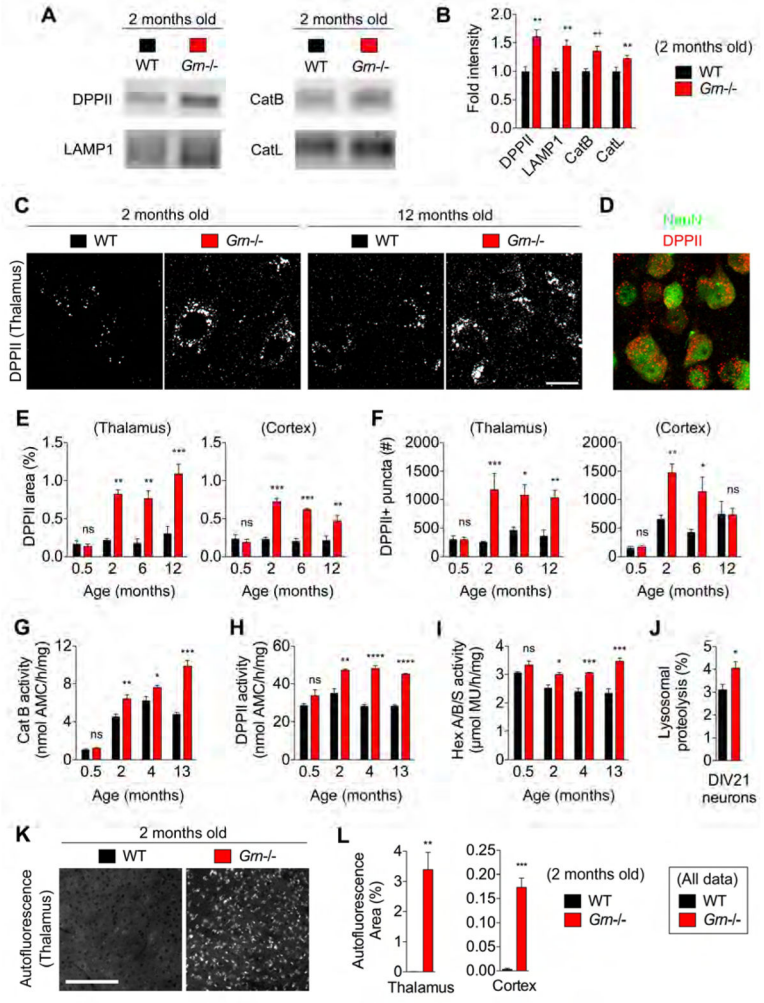

Figure 2. PGRN deficiency causes early and sustained lysosomal enzyme dysregulation

(A) Representative immunoblots with anti-DPPII, LAMP1, CatB, and CatL antibodies using 2-month-old WT and *Grn−/−* mice.

(B) Quantification of immunoblots from (A). Mean ± sem, n = 5–7/group, *p < 0.05, **p < 0.01, ***p < 0.001; Unpaired T-test.

(C) Representative confocal images of thalamus stained with anti-DPPII antibody at 2 months and 12 months of age. Bar, 6 μm.

(D) A representative confocal image of double immunostaining using anti-DPPII and anti-NeuN antibodies.

(E) Quantification of DPPII-immunoreactive area (%) in thalamus and cortex of P15 and 2-, 6-, and 12-month-old WT and *Grn−/−* mice. Mean ± sem, n = 3–5/group, *p < 0.05, **p < 0.01, ***p < 0.001; One-way ANOVA comparing WT vs. *Grn−/−* at 2 months, 6 months, and 12 months separately with Sidak's *post hoc* multiple comparisons test.

(F) Quantification of the number of DPPII-positive puncta in thalamus and cortex of P15 and 2-, 6-, and 12-month-old WT and *Grn−/−* mice. Mean ± sem, n = 3–5/group, *p < 0.05, **p < 0.01, ***p < 0.001; One-way ANOVA comparing WT vs. *Grn−/−* at 2 months, 6 months, and 12 months separately with Sidak's *post hoc* multiple comparisons test.

(G) CatB activity using WT and *Grn*−/− brain lysates at P15 and 2, 4, and 13 months of age. Mean ± sem, n = 4/group, *p < 0.05, **p < 0.01, ***p < 0.001; Unpaired T-test.
(H) DPPII activity using WT and *Grn*−/− brain lysates at P15 and 2, 4, and 13 months of age. Mean ± sem, n = 4/group, *p < 0.05, **p < 0.01, ***p < 0.001; Unpaired T-test.
(I) Hex A/B/S activity using WT and *Grn*−/− brain lysates at P15 and 2, 4, and 13 months of age. Mean ± sem, n = 4/group, *p < 0.05, **p < 0.01, ***p < 0.001; Unpaired T-test.
(J) Lysosomal proteolysis (%) in DIV21 WT and *Grn*−/− cortical neurons. Mean ± sem, n = 8–16 embryos from 2–5 mice/group, *p < 0.05; Unpaired T-test.
(K) Representative images of autofluorescence using 488 nm excitation in thalamus of 2-month-old WT and *Grn*−/− mice. Bar, 50 μm
(L) Quantification of fractional area (%) occupied by autofluorescent puncta measured in (K). Mean ± sem, n = 4–5/group, *p < 0.05, **p < 0.01, ***p < 0.001; Unpaired T-test.

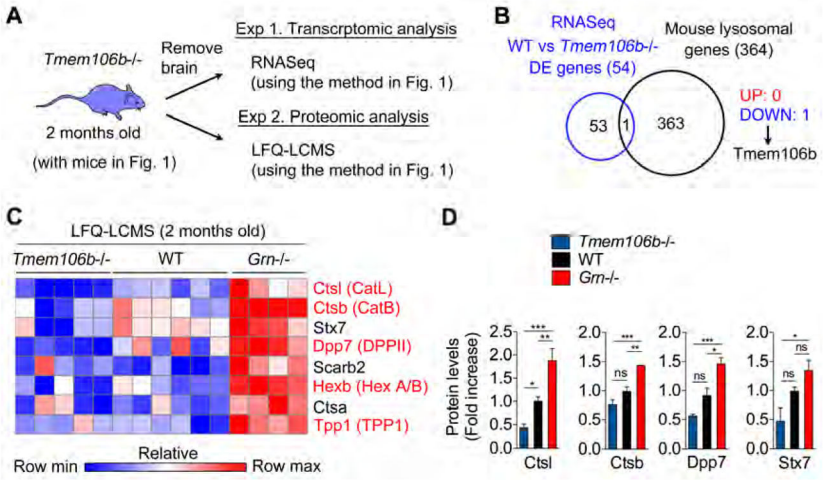

Figure 3. LFQ-LCMS analysis reveals bidirectional control of the lysosome in *Tmem106b*−/− vs. *Grn*−/− mice

(A) Diagram showing the experimental procedures of transcriptomic and proteomic analyses using *Tmem106b*−/− animals.

(B) Venn diagram showing the overlap between differentially expressed (DE) genes (WT vs *Tmem106b*−/−) identified by RNASeq and mouse lysosomal genes.

(C) Heatmap prepared in Gene-E demonstrating a pattern of bidirectional control of the lysosome in *Tmem106b*−/− vs. *Grn*−/− as compared to WT at 2 months of age. Relative scale is shown below. Data is row-normalized.

(D) Bar graphs generated from LFQ-LCMS analysis. Mean ± sem, *p < 0.05, **p < 0.01, ***p < 0.001; One-way ANOVA with Dunnett's *post hoc* test.

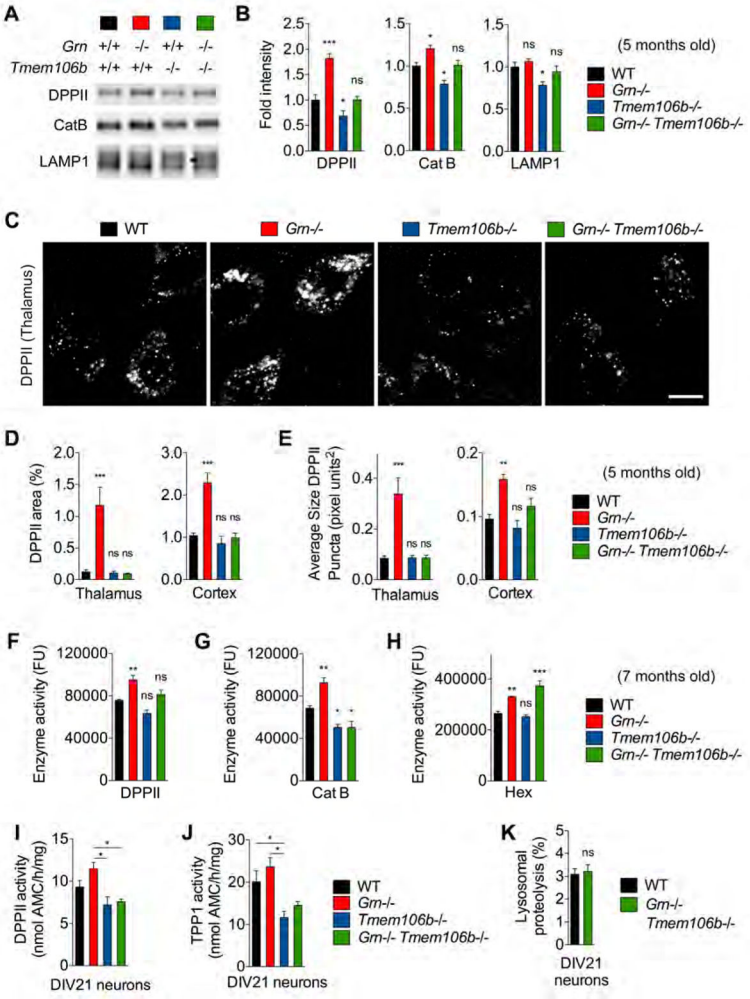

Figure 4. *Tmem106b* deletion rescues lysosomal enzyme dysregulation in *Grn*−/− mice

(A) Representative immunoblots with anti-DPPII, LAMP1, and CatB antibodies using total forebrain lysates from 5-month-old WT, *Grn*−/−, *Tmem106b*−/−, and *Grn*−/− *Tmem106b*−/− mice.

(B) Quantification of immunoblots from (A). Mean ± sem, n = 5–8/genotype, *p < 0.05, **p < 0.01, ***p < 0.001; One-way ANOVA with Dunnett's *post hoc* test.

(C) Representative confocal images of thalamus and cortex in WT, *Grn*−/−, *Tmem106b*−/− and *Grn*−/− *Tmem106b*−/− mice stained with anti-DPPII antibody at 5 months of age. Bar, 6 μm.

(D) Quantification of DPPII-immunoreactive area (%) in thalamus and cortex of 5-month-old WT, *Grn*−/−, *Tmem106b*−/−, and *Grn*−/− *Tmem106b*−/− mice. Mean ± sem, n = 5/genotype, *p < 0.05, **p < 0.01, ***p < 0.001; One-way ANOVA with Dunnett's *post hoc* test.

(E) Quantification of the average size of DPPII-positive puncta in thalamus and cortex of 5-month-old WT, *Grn*−/−, *Tmem106b*−/−, and *Grn*−/− *Tmem106b*−/− mice. Mean ± sem, n = 5/genotype, *p < 0.05, **p < 0.01, ***p < 0.001; One-way ANOVA with Dunnett's *post hoc* test.

(F) DPPII activity using 7-month-old WT, *Grn*−/−, *Tmem106b*−/−, and *Grn*−/− *Tmem106b*−/− brain lysates. Mean ± sem, n = 3–4/genotype, *p < 0.05, **p < 0.01, ***p < 0.001; One-way ANOVA with Tukey's *post hoc* test.

(G) CatB activity using 7-month-old WT, *Grn*−/−, *Tmem106b*−/−, and *Grn*−/− *Tmem106b*−/− brain lysates. Mean ± sem, n = 3–4/genotype, *p < 0.05, **p < 0.01, ***p < 0.001; One-way ANOVA with Tukey's *post hoc* test.

(H) Hex A/B/S activity using 7-month-old WT, *Grn*−/−, *Tmem106b*−/−, and *Grn*−/− *Tmem106b*−/− brain lysates. Mean ± sem, n = 3–4/genotype, *p < 0.05, **p < 0.01, ***p < 0.001; One-way ANOVA with Tukey's *post hoc* test.

(I) DPPII activity using DIV21 WT, *Grn*−/−, *Tmem106b*−/−, and *Grn*−/− *Tmem106b*−/− cortical neurons. Mean ± sem, n = 6–13 embryos from 2–4 mice/genotype, *p < 0.05; One-way ANOVA with Tukey's *post hoc* test.

(J) TPP1 activity using DIV21 WT, *Grn*−/−, *Tmem106b*−/−, and *Grn*−/− *Tmem106b*−/− cortical neurons. Mean ± sem, n = 6–13 embryos from 2–4 mice/genotype, *p < 0.05; One-way ANOVA with Tukey's *post hoc* test.

(K) Lysosomal proteolysis (%) of DIV21 WT and *Grn*−/− *Tmem106b*−/− cortical neurons. Mean ± sem, n = 7–16 embryos from 2–5 mice/genotype, *p < 0.05; Unpaired T-test. This experiment was performed simultaneously with Fig. 2J. The WT group value is therefore identical to Fig. 2J.

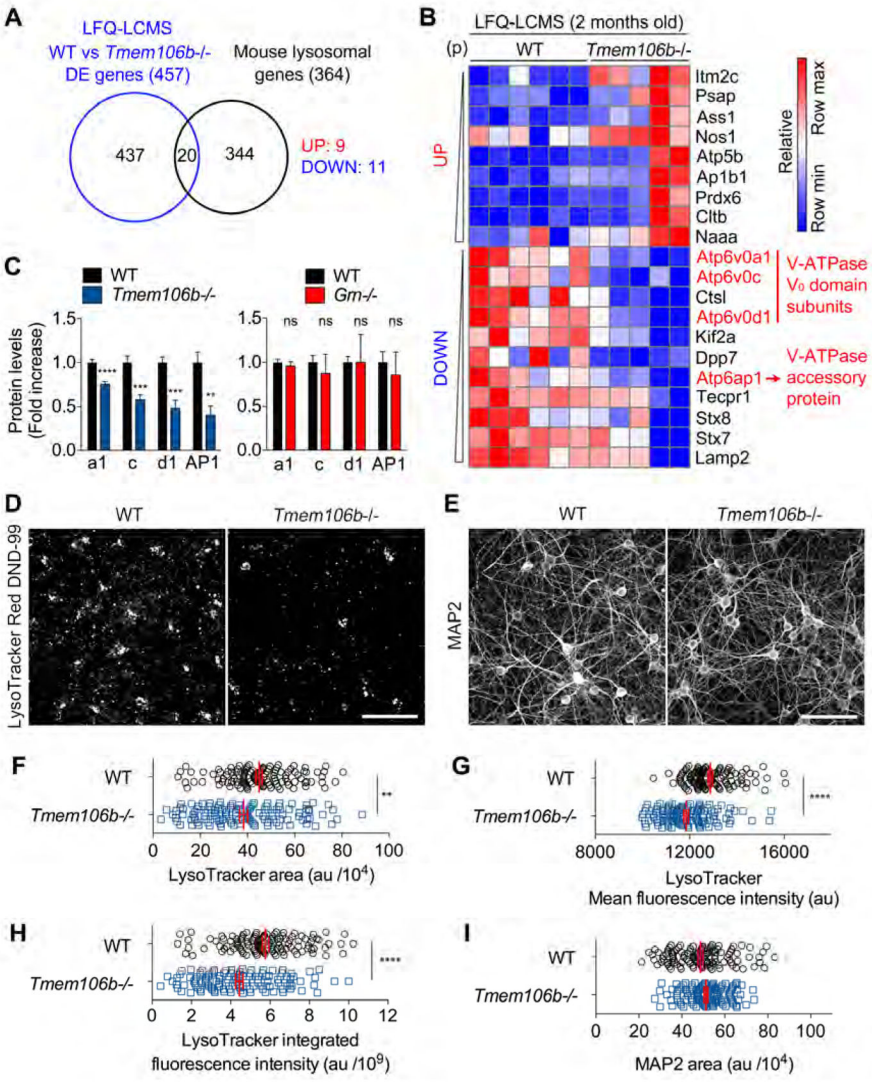

Figure 5. TMEM106B deficiency causes impairment in lysosomal acidification

(A) Venn diagram showing the overlap between differentially expressed (DE) genes (WT vs *Tmem106b*−/−) identified by LFQ-LCMS and mouse lysosomal genes.

(B) Heatmap from Gene-E showing the common 9 upregulated and 11 downregulated genes identified in (A) using LFQ-LCMS dataset ($P < 0.05$, ranked by p value). Relative scale is represented below. Data are row-normalized.

(C) Bar graphs generated from LFQ-LCMS analysis. Mean ± sem. **p < 0.01, ***p < 0.001, ****p < 0.0001.

(D) Representative images of WT and *Tmem106b*−/− primary cultured cortical neurons stained with LysoTracker Red DND-99. Bar, 100 μm.

(E) Representative images of WT and *Tmem106b*−/− primary cultured cortical neurons stained with anti-MAP2 antibody. Bar, 100 μm.

(F) A representative result of quantification of LysoTracker-Red-DND-99-positive area in WT and *Tmem106b*−/− cortical neurons. Mean ± sem, n = 120 sites (from 30 wells)/group, **p < 0.01; Unpaired T-test. Similar results are obtained from 3 independent experiments.

(G) A representative result of quantification of mean fluorescence intensity within LysoTracker-positive area of WT and *Tmem106b*−/− cortical neurons. Mean ± sem, n = 120 sites (from 30 wells)/group, ****p < 0.0001; Unpaired T-test. Similar results are obtained from 3 independent experiments.

(H) A representative result of quantification of integrated fluorescence intensity of LysoTracker-positive area in WT and *Tmem106b*−/− cortical neurons. Mean ± sem, n = 120 sites (from 30 wells)/group, ****p < 0.0001; Unpaired T-test. Similar results are obtained from 3 independent experiments.

(I) A representative result of quantification of MAP2-positive area in WT and *Tmem106b*−/− cortical neurons. Mean ± sem, n = 120 sites (from 30 wells)/group. Similar results are obtained from 3 independent experiments.

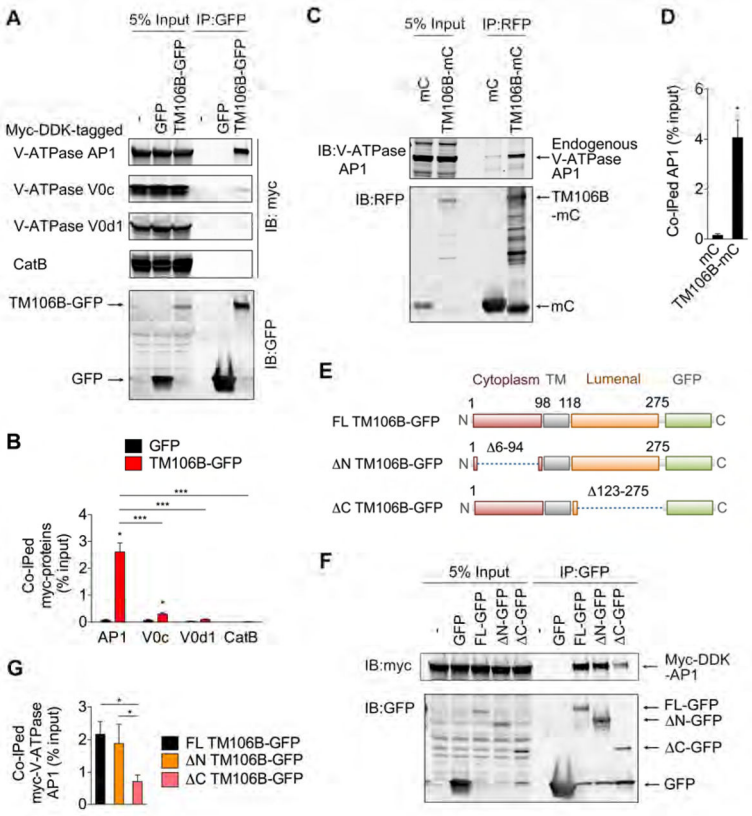

Figure 6. TMEM106B interacts with V-ATPase AP1

(A) Representative blots of co-IP experiments using HEK293T cells expressing GFP or TMEM106B-GFP (TM106B-GFP), together with Myc-DDK-tagged V-ATPase AP1, V0c, and V0d1 and CatB.

(B) Quantification of co-IP in (A). Mean ± sem, n = 3, *p < 0.05; Unpaired T-test (compared with GFP), ***p < 0.01; One-way ANOVA with Tukey's *post hoc* test (between TM106B-GFP IPs).

(C) Representative blots using of co-IP experiments using HEK293T cells expressing mCherry (mC) or TMEM106B-mCherry (TM106B-mC).

(D) Quantification of co-IP in (C). Mean ± sem, n = 4, *p < 0.05; Unpaired T-test.

(E) Schematic drawing of full-length (FL) TM106B-GFP and TM106B-GFP lacking aa6–94 (ΔN) and aa123–275 (ΔC).

(F) Representative blots of co-IP experiments using HEK293T cells expressing GFP, FL TMEM106B-GFP,ΔN TMEM106B-GFP, or ΔC TMEM106B-GFP, together with Myc-DDK-tagged V-ATPase AP1.

(G) Quantification of co-IP in (F). Mean ± sem, n = 3, *p < 0.05; One-way ANOVA with Tukey's *post hoc* test.

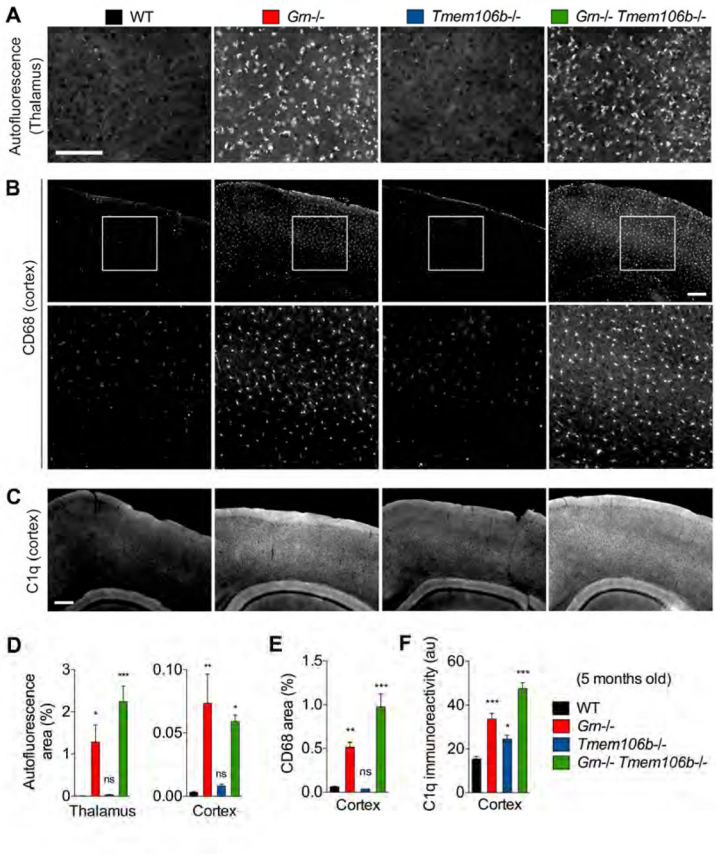

Figure 7. TMEM106B deficiency does not revert accumulation of lipofuscin, CD68-positive microglia, and complement C1q in *Grn*−/− mice

(A) Representative images of autofluorescence using 488 nm excitation in thalamus of 5-month-old WT, *Grn*−/−, *Tmem106b*−/−, and *Grn*−/− *Tmem106b*−/− mice. Bar, 50 μm

(B) Representative images of WT, *Grn*−/−, *Tmem106b*−/−, and *Grn*−/− *Tmem106b*−/− cortex stained for CD68 at 5 months of age. Bottom panels are high-magnification of white square area in top panels. Bar, 200 μm.

(C) Representative images of WT, *Grn*−/−, *Tmem106b*−/−, and *Grn*−/− *Tmem106b*−/− cortex stained for C1q at 5 months of age. Bar, 200 μm.

(D) Quantification of autofluorescent puncta area (%) in 5-month-old WT, *Grn*−/−, *Tmem106b*−/−, *Grn*−/− *Tmem106b*−/− mice. Mean ± sem, n = 4–5/group, *p < 0.05, **p < 0.01, ***p < 0.001; One-way ANOVA with Dunnett's *post hoc* test.

(E) Quantification of C1q-immunoreactivity in WT, *Grn*−/−, *Tmem106b*−/−, and *Grn*−/− *Tmem106b*−/− cortex. Mean ± sem, n = 3–5/group. *p < 0.05, ***p < 0.001; One-way ANOVA with Dunnett's *post hoc* test.

(F) Quantification of CD68-immunoreactive area (%) in WT, *Grn*−/−, *Tmem106b*−/−, and *Grn*−/− *Tmem106b*−/− cortex. Mean ± sem, n = 3–5/group. *p < 0.05, ***p < 0.001; One-way ANOVA with Dunnett's *post hoc* test.

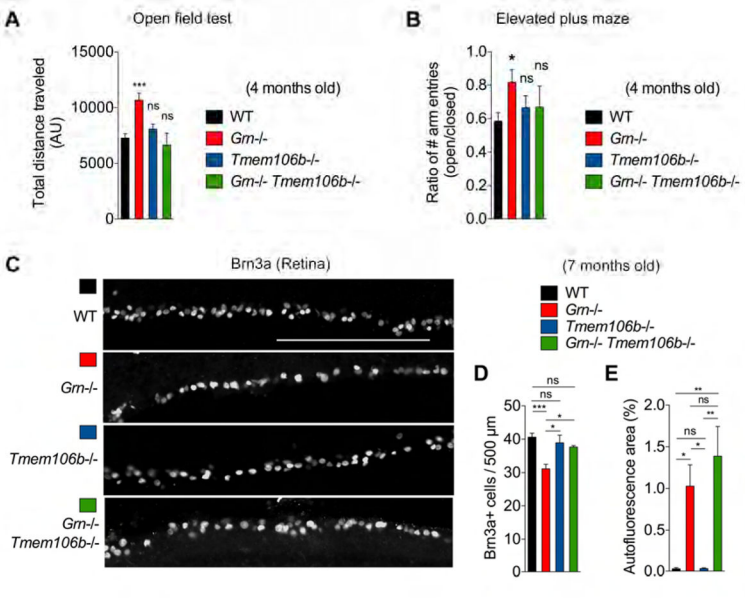

Figure 8. *Tmem106b* deletion rescues behavioral abnormalities and retinal ganglion cell degeneration in *Grn*−/− mice

(A) Open field test results at 4 months of age showing total distance traveled, a measure of locomotor activity. Mean ± sem, n = 8–27/genotype, *p < 0.05, **p < 0.01, ***p < 0.001; One-way ANOVA with Dunnett's *post hoc* test.

(B) Elevated plus maze at 4 months of age showing ratio of number of entries into the open vs. closed arms of the maze. Mean ± sem, n = 8–27/genotype, ***p < 0.001; One-way ANOVA with Dunnett's *post hoc* test.

(C) Representative images of WT, *Grn*−/−, *Tmem106b*−/−, and *Grn*−/− *Tmem106b*−/− mouse retinas stained for Brn3a at 7 months of age. Bar, 250 µm.

(D) Quantification of Brn3a-positive cells/500 µm in 7-month-old WT, *Grn*−/−, *Tmem106b*−/−, and *Grn*−/− *Tmem106b*−/− retinas. Measurements were taken in the central regions of the retina. Mean ± sem, n = 3–4/group. *p < 0.05, ***p < 0.001; One-way ANOVA with Tukey's multiple comparisons *post hoc* test.

(E) Quantification of autofluorescence area (%) in 7-month-old WT, *Grn*−/−, *Tmem106b*−/−, and *Grn*−/− *Tmem106b*−/− retinas. Measurements were taken in the central regions of the retina. Mean ± sem, n = 3–4/group. *p < 0.05, ***p < 0.001; One-way ANOVA with Tukey's multiple comparisons *post hoc* test.